X-Ray Analysis of YSO candidates near SNR HB9

Master's Thesis in Physics

Presented by

Kyle Marshall

September 28, 2018

Friedrich-Alexander-Universität Erlangen-Nürnberg

Supervisor: Dr. Manami Sasaki

Table of Contents

CHAPTER 1: INTRODUCTION TO SNRS AND YSOS IN X-RAY ASTRONOMY 4

1.1 STELLAR EVOLUTION 4

1.2 THE CATACLYSMIC FINALE: SUPERNOVAE AND SHOCKWAVES 11

1.3 SNR HB9 AND SH2-219 18

1.4 XMM-NEWTON OVERVIEW 21

CHAPTER 2: METHODOLOGY 24

2.1 GOOD TIME INTERVAL FILTERING 24

2.2 RGB IMAGES 25

2.3 X-RAY SOURCE DETECTION 26

2.4 MULTI-OBSERVATION LIGHT CURVES OF SUSPECTED SOURCES 30

2.5 OPTICAL/NIR SOURCE COUNTERPARTS 30

2.6 SPECTRAL ANALYSIS OF BRIGHTEST X-RAY SOURCES 35

CHAPTER 3: RESULTS AND ANALYSES 40

3.1 MAIN SEQUENCE FOREGROUND STARS 46

3.2 YSO CANDIDATES 50

3.3 UNCLASSIFIED/BINARY SYSTEM X-RAY SOURCES 57

3.4 NON-SOURCES 62

CHAPTER 4: DISCUSSION 64

REFERENCES 68

APPENDIX A 73

APPENDIX B 80

APPENDIX C 97

CHAPTER 1: Introduction to SNRs and YSOs in X-Ray Astronomy

X-ray astronomy, albeit a relatively new method of probing the universe, has been proving itself to be a missing puzzle piece in analyzing and understanding the universe's most violent and energetic events – supernovae (SNe). Furthermore, x-ray analysis provides insight into young stellar objects (YSOs) and whether or not the high energy outflow (shocks) from SNe has any effect on a young star's development.

It was first discovered in the early 1980's by the Einstein observatory that X-rays were emitted in YSOs, specifically T Tauri stars (Montmerel et al. 1983). This discovery came as a *shock* to the astronomical community, as it was believed that only main sequence stars possess the temperatures necessary to emit X-rays. The mechanisms through which YSOs produce X-rays will be discussed in section 1.1.2.

1.1 Stellar Evolution

The development and lifecycle of a star is a complex process with many of the early stage 'triggers' of star formation not being well understood. As a star begins its lifecycle it is initially quite cool, and in time, accumulates more mass and increases its core temperature, thus igniting hydrogen fusion within the star's core. It is due to their relatively low temperatures that caused the detection of x-rays from YSOs to come as a surprise to astronomers. The detection of X-rays from YSOs point to alternative production mechanisms other than thermal radiation.

1.1.1 Star Formation

Star forming regions are areas of space that contain dense molecular clouds of gas and dust. The majority of the interstellar medium (ISM) is hydrogen gas (~70% by mass) and helium. This interstellar cloud has been chemically enriched with heavier elements from the ejecta of stars which had passed their main sequence and ended in a colossal supernova explosion. The process by which this chemical enriching happens will be discussed in more detail in later sections. The molecular cloud can remain in equilibrium and resist gravitational collapse only if the cloud's internal pressure is large enough. This pressure-gravity equilibrium relationship can be described mathematically by the viral theorem, $\langle T \rangle = -\frac{1}{2}\sum_{i=1}^{N} F_i \cdot r_i$. That is, if we describe the cloud as a system of N particles, one finds that the gravitational potential must be equal to twice the internal thermal energy for the cloud to remain in equilibrium. Once the molecular cloud accumulates a certain amount of mass, known as the Jeans mass, the cloud will undergo gravitational collapse and star formation will begin. The value for the Jeans mass is not static, it depends on both the density and temperature of the cloud.

As discussed, star formation can happen on its own as matter accumulates, but it can also be triggered by external sources such as SN explosions or the collision with another molecular cloud. As gravitational collapse continues, a protostar cloud develops. The cloud's material heats up to temperatures on the upwards of 100K, where it radiates most of its energy in the infrared wavelengths.

1.1.2 Young Stellar Objects (YSOs)

Young stellar objects, as the name implies, are stellar bodies which are very early in their developmental cycle. Unlike stars on the main sequence, which are powered and sustained by nuclear fusion within the stellar core[1], YSOs are powered solely by gravitation potential energy released during gravitational collapse. These young stars, on their way to developing into main sequence stars, show strong variability and emission in the X-ray wavelengths. The detection of X-rays in YSOs was a shocking discovery for the astronomical community, because it had been assumed that the environment of a YSO, without the assistance of a high-velocity shockwave, was too cold to be active in the X-ray regime. The Einstein observatory's discovery opened the door for the expansion of humanity's understanding of the processes involved in the early stages of stellar evolution.

YSOs are most commonly assigned a class according to their spectra. The system analyzes the slope of the object's spectrum and then allows a YSO to be grouped in one of four classifications: Class 0 and Class I protostars, Class II (Classical) and Class III (Weak-line) T Tauri stars (TTS).

Class 0 protostars are defined as having most of their mass not yet assembled. That is, most of the protostar's mass is located in the envelope and has yet to fall inward,

[1] This nuclear fusion is of course a result of the heating of the stellar core due as a result of the immense gravity. Main sequence stars and PMS stars/YSOs are both 'powered by gravity' so to speak, the distinction is that the radiation from main sequence stars is a direct result of nuclear fusion, whereas this is not true for PMS stars/YSOs.

onto the star. The spectrum of a Class 0 protostar is very narrow, resembling that of a single temperature blackbody at $T \leq 30\ K$ (M. Barsony 1994 [1]). After some millions of years, the steady inflow of material will have raised the density of the stars core. Once the core's temperature, which has been steadily increasing due to the contraction of the star, reaches a critical value, the internal pressure will be strong enough to resist further gravitational collapse. This state is referred to as hydrostatic equilibrium and marks the beginning of the Class I protostar phase.

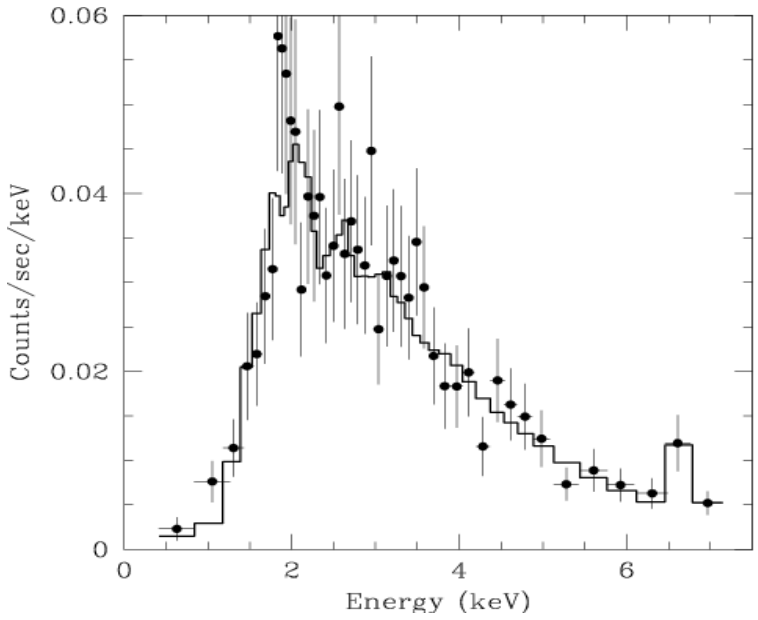

Figure 1: Energy spectrum of EC 95, a young stellar object between a very young Class I and a later stage Class II. (Image taken from Preibisch 2003 [2]).

Following the protostar phase of stellar evolution, a star with mass fewer[2] than two solar masses becomes a so-called T Tauri star. These young stars show strong X-ray emission and variability, with X-ray luminosity being orders of magnitude greater

[2] A star with mass between 2 and 8 solar masses becomes a Herbig Ae/Be star, and anything beyond 8 solar masses has no premain sequence stage following the protostar stage.

than main sequence stars of similar mass (M. Jardine et al. 2005 [3]). During this stage, the star's surface temperature is comparable to that of a main sequence star; however, the TTS are much more luminous due to their larger radii. These stars are not powered by fusion due to their core's temperature being too low, instead the stars are fueled by the gravitational energy that is released as the stars contract further and move toward the main sequence.

1.1.2.1X-ray Production in YSOs: Outflow Jets and Wind-Shock Model

The first theorized model to be discussed for X-ray production in YSOs is the 'wind-shock model'. Observations of star-forming regions show high velocity bipolar outflows produced by Class 0 and Class I protostars (Reipurth & Bally [4]). These bipolar outflows can reach velocities of 100-700 km/s, which highly supersonic. When this material collides with the surrounding interstellar cloud, shockwaves are produced and the ISM is heated to temperatures in excess of 1 MK, causing it to radiate soft X-rays.

The outflow jets observed in the Class 0 YSOs up to (but not including) the WTTS phase are theoretically described as collimated disk winds with hydromagnetic properties. The strong magnetic field of the rotating YSO imparts a torque onto these winds, which essentially extracts angular momentum and gravitational potential energy from the disks (Pudritz et al. 2006 [5]). Two essential ingredients in the magnetic dynamo process is a convection zone, present in cooler stars, and (differential) rotation (Stelzer 2017 [6]). Due to YSOs having a faster rotation as compared to MS stars, the

X-ray activity is significantly higher (specifically during the Class I and Class II stages). the X-ray luminosity detected from TTS can reach 10^3 orders of magnitude larger than from MS dwarfs (Stelzer & Neuhäuser 2001 [7]).

These outflowing jets are closely tied to the young star's accretion disk, so much so that once the circumstellar disk has vanished, the jets disappear as well. The YSO's toroidal magnetic field lines is a result of the rotation of the conducing gas of the circumstellar disk. Goodson and Winglee (1999 [8]) theorized a jet-launching mechanism which proposes that magnetic field lines which connect to the disk and star become intertwined and form a helical structure. The magnetic interaction between the disk's magnetic structure and the YSO's core can be studied by examining how magnetic helicity is transferred between the interacting parts. Helicity injection causes these magnetic connection loops to expand. The paper elaborates on this process by stating that the expansion of these magnetic field lines, in conjunction with the axial symmetry of the stellar disk, drives the bipolar outflows along the star's axis of rotation. From the equations of ideal magnetohydrodynamics (MHD), Pudritz et al. (2006 [5]) derive an insightful scaling relation between the jet outflow rates and the accretion rates:

$$\dot{M}_a \cong \left({}^{r_a}/_{r_o}\right)^2 \dot{M}_W \qquad (1)$$

where $\dot{M}_a$ is the mass accretion rate, $\dot{M}_W$ is the mass outflow rate, r_0 is the radius to a point on the disk, r_a is the Alfvén radius[3], and ${}^{r_a}/_{r_o}$ is a leaver arm ratio of the flow. Through numerical work, the lever arm ratio in YSOs is commonly found be ${}^{r_a}/_{r_o} \cong 3$.

[3] The Alfvén is defined as the radial distance at which the magnetic energy density is equal to that of the kinetic energy density.

Henceforth, we obtain the relation $\dot{M}_W/\dot{M}_a \cong 0.1$ which has been observationally verified in many YSO systems.

1.1.2.2X-ray Production in YSOs: Accretion Shocks

The rotating accretion disk material of the YSO is confined within its toroidal magnetic field due to it being an electrically conducting fluid (plasma). As this magnetically confined matter accretes onto the star's surface (onto the magnetic poles) at supersonic velocities, shockwaves form, heating the plasma to X-ray producing temperatures (>1MK). The terminal velocity of the accreting mater, v_m, can be calculated:

$$v_m \cong 0.8\left(\frac{2GM_*}{R}\right)^{\frac{1}{2}} \cong 495\left(\frac{M}{M_\odot}\right)^{\frac{1}{2}}\left(\frac{R}{R_\odot}\right)^{-\frac{1}{2}} [\text{km s}^{-1}] \text{ [9]} \qquad (2)$$

The factor of ≈ 0.8 arises from considering that the falling matter will most likely not straight lines but instead will follow curved magnetic field lines down to the stellar surface (Guedel & Naze 2009 [9]). According to shock theory, the accretion formed shock waves for a typical TTS reaches temperatures of $T_s \approx (0.4 - 4) \cdot 10^6$ K, which is in the electron temperature range in which one would expect soft X-ray production.

1.1.3 X-Ray Emission from Main-Sequence Stars

X-ray production in cool MS stars (stars to the right of Class A on a Hertzsprung-Russel diagram), such as our sun, is a result of thermal emission from hot, magnetically confined coronal plasma. This confined plasma is as a result of the interaction between the cool star's convection zone and the stellar rotation – a magnetic dynamo.

1.2 The Cataclysmic Finale: Supernovae and Shockwaves

During the final stages of a star's life it enters a nonequilibrium state which is initiated by one of two possible over-arching triggering mechanisms: thermal runaway and gravitational collapse (section 1.2.1).

SNe can be further classified into types by their chemical composition, deduced from the measured elemental absorption lines in the optical spectrum, but the primary classification system for SNe is according to the triggering mechanism which caused it – thermal runaway or gravitational collapse. SNe can be classified as type-I if the progenitor star does not contain any hydrogen, or type-II if the progenitor contains hydrogen. Within these general type-I and type-II classes, SNe can be again further classified according to the measured absorption lines. It is worth noting that type-Ia SNe are a result of thermal runaway, whereas all other types are born out of gravitational collapse.

Type-Ia SNe show a strong ionized silicone line (Si II), whereas type-Ib/c show weak or no traces of silicone absorption. Type-Ib and type-Ic SNe are distinguished from each other according to their helium content. Type-Ib shows a helium line (He I) and conversely, type-Ic shows weak or no amounts of helium.

Type-II SNe are not classified so much by elemental composition as is the case for type-I, instead they are classified by the shape of their light curve. Type-II-P/L/N SNe have light curves which display a plateau (P), a linear decrease (L), or narrow lines (N). The spectrum of a type-IIb eventually evolves into that of a type-Ib. Recalling the two triggering mechanisms, it is important to note that type-Ia SNe are caused

exclusively by thermal runaway and all other types of SNe are caused by gravitational collapse.

1.2.1 Triggering Mechanisms

The progenitor star and the triggering mechanism by which a supernova forms dictates the supernova type and the elemental composition of the remnant. For example, a star with high metallicity and a mass between 25-40 solar masses will end its life in as type-II SN and leave behind a neutron star, whereas a star with low metallicity and a mass between 40-90 solar masses will undergo core collapse and will collapse into a black hole without having ever become a supernova (Heger et al. 2003).

1.2.1.1 Thermal Runaway

In the event a white dwarf accretes enough matter from a companion star to raise its core temperature high enough to spark carbon fusion, the white dwarf will enter a thermodynamic instability – so-called thermal runaway. This section will touch on the three most common methods in which thermal runaway occurs.

The first cause of thermal runaway to be discussed occurs in the event that a white dwarf with a carbon/oxygen core (C/O WD) with mass close to the Chandrasekhar limit is in a binary system with a main sequence star. The white dwarf can accrete mass from the evolved companion star, and over some time the increased compressional pressure ignites an explosion near the white dwarf's center (Höflich & Stein 2002 [10]).

Alternatively, there is the possibility for a white dwarf to runaway thermodynamically even if it does not have a mass close to the Chandrasekhar limit. Consider a binary system comprised of two low mass, white dwarfs. General relativity states that due to gravitational radiation, the white dwarf pair loses angular momentum and the separation distance between these two stars' centers gradually decreases until the two stars merge; the combined mass and pressure resulting from the collision of the two stars is enough to ignite carbon fusion and produce the thermodynamic runaway.

Lastly, a low mass C/O WD can enter the runaway phase due to an ignition in the stars outer helium layer (Sugimoto & Nomoto 1980 [11]). This explosion in the outer layer propagates into the core, raising temperatures enough to disrupt the thermodynamic stability of the star, sending it into runaway.

1.2.1.2 Gravitational Collapse

As mentioned before, gravitational collapse is the triggering mechanism for every type of SN other than type-Ia. Iron core collapse is initiated through photodisintegration and electron capture within the iron core. During the collapse process, the star's diameter will shrink, and the accumulated gravitational energy from stellar compression will be radiated outward from the star. A star undergoing gravitational collapse will continue to do so until it reaches a new state of equilibrium. Such equilibriums include core collapse with little radiation into a neutron star or a black hole, or the star could go out with a bang in the form of a supernova.

Photodisintegration, one of the triggers for SNe through core collapse, can occur when the cores temperatures become sufficiently hot to radiate highly energetic gamma

rays. These gamma-rays can be absorbed by the iron in the core which are then kicked into highly excited states, immediately following is a decay of the excited atom by the emission of a subatomic particle. During this endothermic process, energy is drawn from the core and collapse is initiated.

This collapse can end in few different ways depending on the star's physical parameters: If the star does not have sufficient mass for its core to explode, or more clearly phrased, if the gravitational energy released is less than the binding energy of the core, a new equilibrium state can be reached in the form of a neutron star or a black hole with having radiated little of the core's energy; the star's outer layers will be expelled in the form of a faint type-II supernova. In the event that the core collapses in a neutron star, the gravitational forces are balanced by neutron degeneracy pressure. If the star is more massive a proper supernova will form and the stellar core will explode [4].

1.2.2 Shockwaves

Shockwaves occur when a wave propagates through a medium faster than the local speed of sound. Shockwaves carry energy just as any other wave, however an important characteristic of shockwaves is their sudden and almost discontinuous, change in pressure, temperature, and density of the medium (Figure 2). Shocks are frequently occurring astrophysical events despite the ambient densities of the ISM being low.

[4] Of course there are exceptions to this generalized statement, as core collapse is an extremely complex process that depends on a number of physical parameters other than mass - an important one being metallicity content (section 1.2).

Given the low density conditions, the shockwaves are collision-less. That is, the interaction between shock and matter is not governed by 2-body coulomb collisions. The reason for this is due to the mean path of these collisions being extremely large and possibly exceeding the system size. Instead, the shock-matter interaction is a result of the collective interaction of fields whose interaction length in generally agreed upon to be on the order of so-called Debye length. In astrophysical environments such as plasma in the ISM, electron densities are low and as a result, we obtain macroscopic values for the Debye lengths:

Plasma	Electron density (m^{-3})	Temperature (K)	Magnetic field (T)	Debye length (m)
Gas discharge	10^{16}	10^{4}	–	10^{-4}
Tokamak	10^{20}	10^{8}	10	10^{-4}
Ionosphere	10^{12}	10^{3}	10^{-5}	10^{-3}
Magnetosphere	10^{7}	10^{7}	10^{-8}	10^{2}
Solar core	10^{32}	10^{7}	–	10^{-11}
Solar wind	10^{6}	10^{5}	10^{-9}	10
Interstellar medium	10^{5}	10^{4}	10^{-10}	10
Intergalactic medium	1	10^{6}	–	10^{5}

Table 1: Electron density, temperature, magnetic field, and the Debye length corresponding to various astrophysical phenomena. Source: The Particle Kinetics of Plasma (Chapter 20) [12]

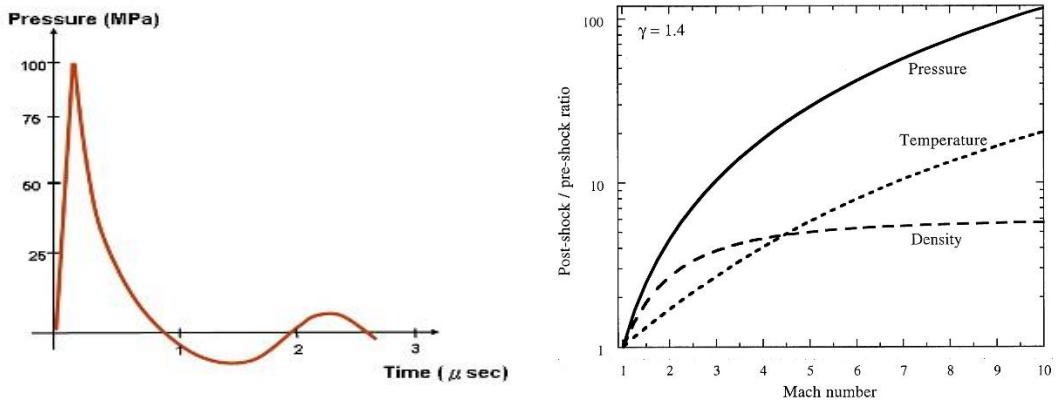

Figure 2: (Left) Pressure-time profile of a highly supersonic shockwave (source: https://www.wikilectures.eu/w/Shock-wave#/media/File:Pressure_plot.png). Notice the drastic pressure increase in a small amount of time. (Right) Pre-post shock ratios corresponding to different Mach number shocks for common fluid parameters: density, temperature, and pressure (source: Connolly & Love 1998 [13]).

1.2.2.1 Hydrodynamics of Shockwaves

Shock waves are disturbances that propagate in a medium faster than the local speed of sound. This speed of sound in a fluid[5] is governed by its physical parameters, namely the compressibility (dependent on molecular structure of the fluid) and the density. The other dynamic parameters can be derived from thermodynamic relationships. The molecular weight of the medium affects the local speed of sound such that heavier gases result in a slower speed of sound whereas in light gases, sound waves can propagate much faster. This relationship should not come as a surprise if we briefly examine what's occurring at the molecular level. Imagine the fluid is homogeneous and that the molecules are connected to one another by small springs, that when perturbed work to restore the system to its steady state. Fluids are different than solids in that they only allow for the propagation of longitudinal (compression) waves (Figure 3). These longitudinal waves travel through a medium by 'squeezing' the particles together, known as compression, which is followed by an expansion of the particles, referred to as rarefaction. The wave travels by temporarily storing and transferring its energy through the spring-like bonds between the molecules. The wave momentarily displaces particles, creating regions of high and low pressure; thus, using this analogy it is reasonable to deduce that particles of large mass will go through compression and rarefaction phases much slower. This of course is an overly simplified view of fluid

[5] The ISM and ejecta to which these shockwaves apply are described as fluids, and so this discussion will be restricted to such.

dynamics but is provides some insight into the fact that the speed of sound decreases with the molecular fluid mass.

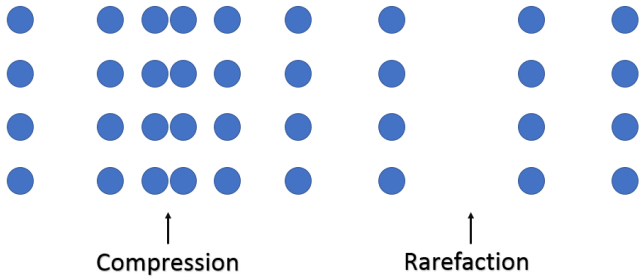

Figure 3: Longitudinal compression waves propagating through a homogeneous medium.

When the local sound limit is exceeded by some 'thing', it results in a disturbance traveling through the medium faster than the medium can react, and this results in the observed, almost instantaneous change in the medium's physical parameters when it encounters the shock front.

1.2.3 Supernova Remnants

During the final titanic explosion of the supernova, the majority of the stellar material is expelled outwards at extremely high velocities, $v \gtrapprox 10^4 \mathrm{km\,s^{-1}}$. This rapidly expanding cloud of ejecta generates shock waves which heat the ejecta and ISM. This expanding region of shocked and heated ISM and ejecta is referred to as a supernova remnant (SNR).

The SNR shockwave continues to expand outwards at a constant velocity over the course of tens or hundreds of years; this is the free expansion phase, the first of several phases a SNR goes through in its lifetime. Two shock waves form – a forward propagating shock which expands out into the ISM, and a reverse shock. The reverse

shock is created by pushing-back on the ejecta caused by the rapid expansion of ambient material that recently experienced the forward shock. The pressure of the expanding ISM eventually exceeds the thermal pressure from the ejecta and creates a reverse shock which propagates back through the SNR (R. Chevalier [14]), shocking the remnant material, causing it to heat and illuminate, almost as if it is revealing itself to us, allowing it to be observed and analyzed for some period of time.

1.3 SNR HB9 and Sh2-219

As previously discussed, when the shock front of a SNR passes through a cold HII region, it causes an extremely rapid change in pressure and temperature of the hydrogen gas, which is theorized to be a mechanism for triggering star formation. The SNR under study, G160.9+2.6 (HB9), has a shock front which appears to be passing through an HII region named Sh2-219 located at (04:56:08.02 +47:23:42.5).

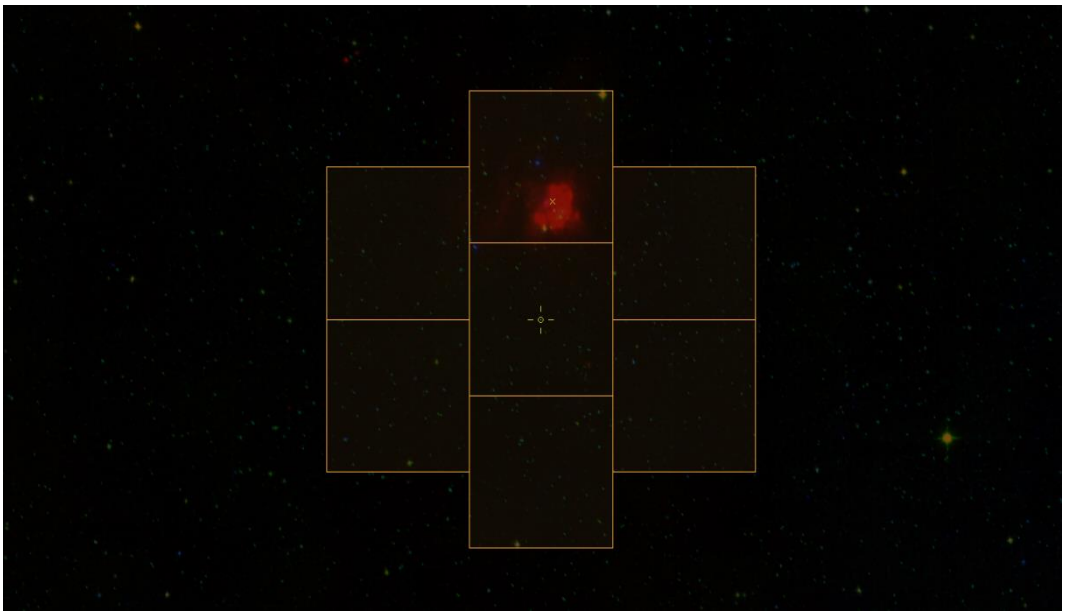

Figure 4: XMM-Newton field of view (yellow boxes) overlaid on a RGB image (red=12um, green=2.16um, blue=0.48um). The red region with the yellow 'x' depicts the HII region Sh2-219. Field of view in this image is approximately 1.3º x 45′

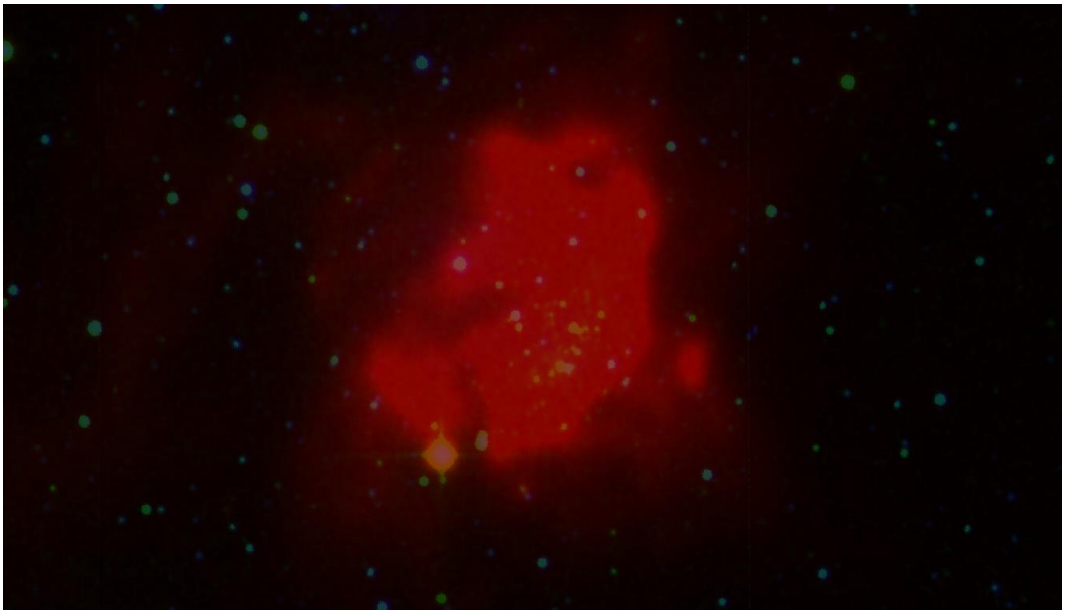

Figure 5: Close-up RGB image of Sh2-219 (RGB values are the same as before). Field of view in this image is approximately 10′ x 6′.

High resolution observations of the 408 MHz, 1420 MHz, and H I-line continuum emission of HB9 were studied by Leahy and Roger [15]. A contour map of

the 1420 MHz continuum emission was produced (Figure 6) which shows the right ascension and declination of HB9 as well as the nearby HII region, Sh219. An accurate estimate of the SNR's distance could not be made from the observation but it was estimated to be at a distance of less than 4 kpc and was suggested that the SNR may be interacting with a pulsar located at 1.8 kpc. The HII region, Sh-219, is located at a distance of 5.0 ± 0.8 kpc with a diameter of 4.4 pc (Deharveng et al. 2003 [16]).

Given this information and Gaia photometric data for the point sources under investigation (discussed in section 2.5), we can estimate if the X-ray sources are located within the HII region Sh-219 and also if they are in the influence area of HB9's shock front.

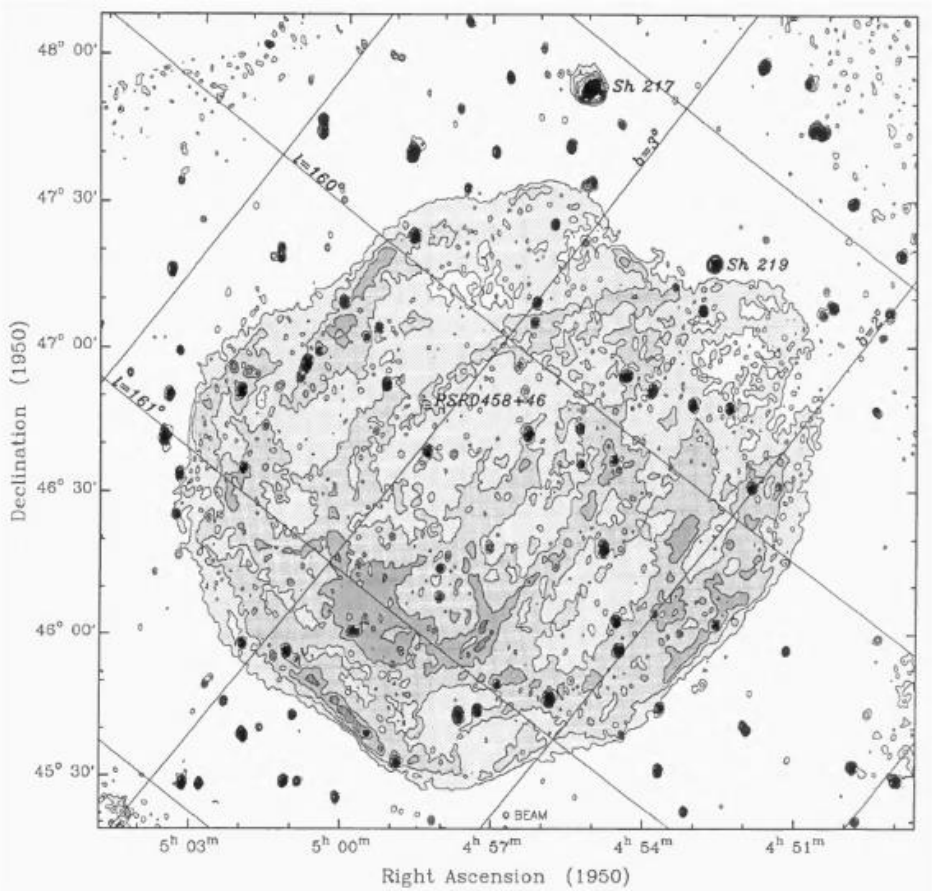

Figure 6: 1420 MHz continuum emission contour with Sh-219 and Sh-217 shown. The contour levels are 1.2 1.7 2.2 2.7 3.2 K brightness temperature. Image taken from Leahy and Roger 1991 [15].

1.4 XMM-Newton Overview

The X-ray multi-mirror mission (XMM-Newton) was the observatory used in the collection of the X-ray data for the area surrounding Sh2-219 (yellow area in Figure 4). XMM-Newton is an X-ray observatory that was launched in 1999 by the European Space Agency (ESA). It is composed of three individual X-ray telescopes, each containing 58 Wolter I grazing-incidence mirrors which are arranged in a coaxial and confocal configuration (ESA [17]). The three telescopes are referred to by the type of CCD from which the camera is made, namely MOS1 (metal oxide semiconductor),

MOS2, and PN; together these combine to form the European Photon Imaging Camera (EPIC).

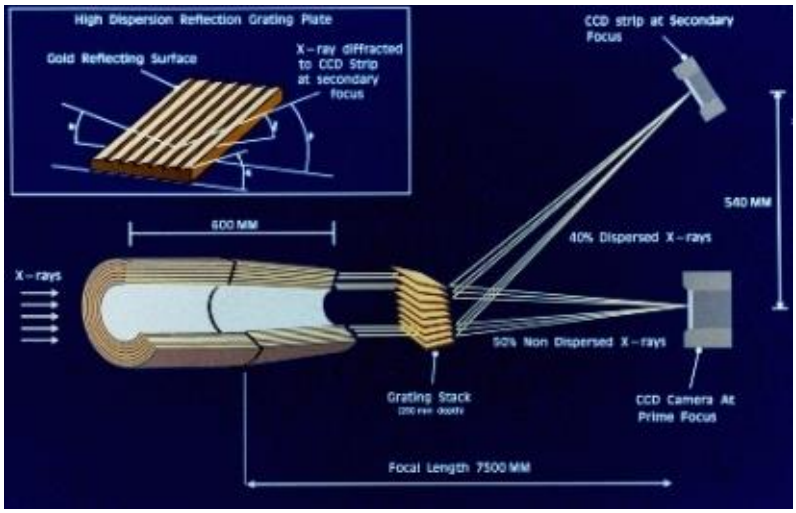

Figure 7: XMM-Newton telescope schematic showing the PN camera at prime focus and one MOS camera at the secondary focus (Image taken from ESA [17]).

The two MOS cameras are formed by an array of 7 MOS CCDs which are installed behind the telescopes' reflection grating spectrometers. Each CCD has an imaging area of approximately 2.5 cm x 2.5 cm, thus, the 7 CCD montage covers an effective area of 62mm in diameter which corresponds to approximately 28.4 arcminutes. Taking into account obstruction losses, approximately 44% of the original flux reaches the MOS cameras. The PN camera, which uses an array of pn CCDs, receives an unobstructed incoming flux and is located at the focal point of the telescope. The quantum efficiencies of each camera must be considered in order to determine the usable energy range for spectral analysis. The European Space Agency produced these quantum efficiency plots for both the MOS and PN instruments. The quantum efficiency of the MOS telescopes fall off sharply at ~8 keV and report <20% efficiency at 10 keV whereas the PN telescope can detect photons up to 15 keV, thus the PN

telescope compensates for the less than optimal quantum efficiency of the MOS camera in the 8-10 keV range. Due to the low efficiency of the MOS cameras for photon energies greater than 10 keV, the spectral analysis of the X-ray sources will cover the 0.2-10 keV range.

CHAPTER 2: Methodology

2.1 Good Time Interval Filtering

The event files must be filtered to obtain the so-called good time interval (GTI). The GTI is the observation time during which the X-ray detection rate remains reasonably constant. Over the course of the observation, the count rate can vary considerably, showing periods where the count rate becomes large very quick, followed by an eventual sharp decline back to 'regular' count rates. These peaks correspond to periods of high background flares. During these periods, the camera's focal plane is predominantly illuminated by low energy protons, thus rendering the low count rate X-rays virtually unanalyzable. The count rate thresholds used for the four observations were 0.40counts/s and 0.35counts/s for the PN and two MOS cameras respectively.

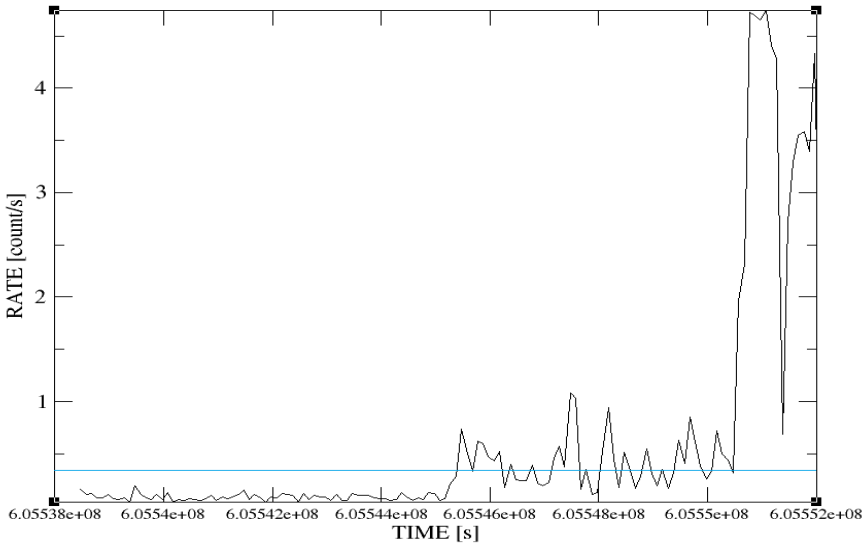

Figure 8: Generated light curve from the raw event list file. The light curve depicted here is belonging to the MOS 1 camera during observation 1. The blue line shows the count rate cut-off limit; any data recorded above this line is discarded.

2.2 RGB Images

In order to get a visual sense of the energy distributions for the entire field of view of these observations, red-green-blue (RGB) color images were prepared (Figure 9). Three different energy band images were created using the XMM-SAS[6] command *evselect* and assigned a color (RGB). The three energy bands used for the color image, in units of kilo-electron volts (keV), were (0.3-1), (1-2), (2-7) which correspond to the colors red, green, and blue respectively. These images were created for all three cameras in each of the four observations. Henceforth, from these images, one can see small luminous points which can be prematurely suspected to be point sources[7]. A predominantly red point signifies a soft X-ray source, whereas a blueish point corresponds to a harder, higher energy X-ray source.

[6] The Science Analysis System (SAS) is a set of computational scripts and libraries which are used in order to process, filter, and analyze data from XMM-Newton missions. The SAS systems allows users to take raw observational data, and after a series of tasks, produce informative images, statistics, and other analytics.

[7] Not all of these small bright points are YSOs/X-ray sources. Determination will made during the analysis section in chapter 3.

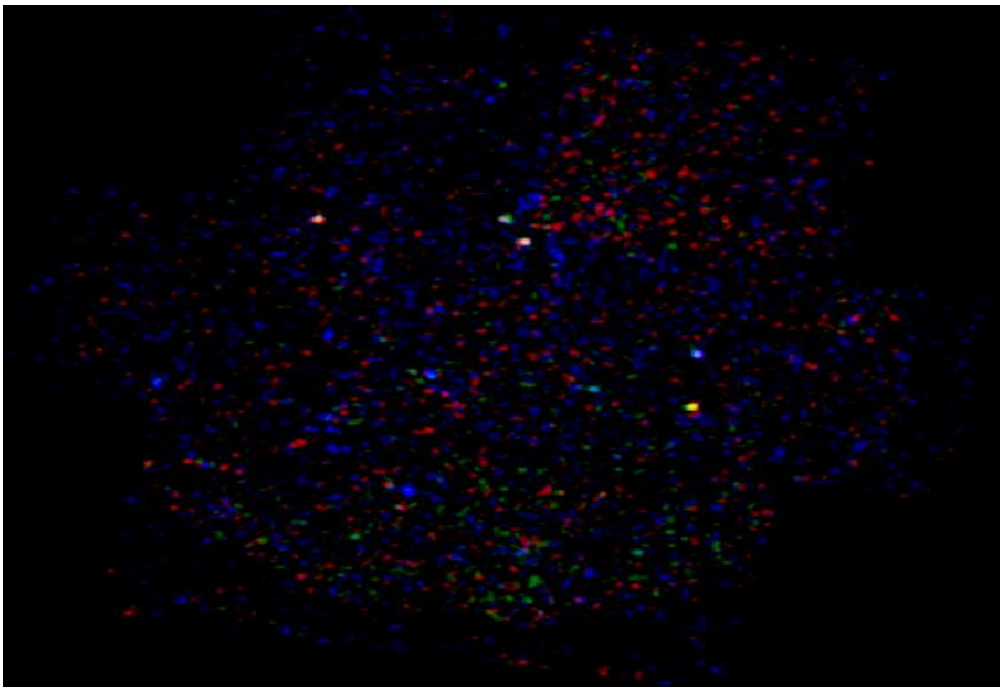

Figure 9: RGB image created from the MOS2 camera during observation 1. The energy bands (0.3-1), (1-2), (2-7) keV correspond to colors red, green, and blue, respectively.

2.3 X-ray Source Detection

The RGB images prove useful for a visual description of the energy distribution throughout the detectors' fields of view. From these images one can speculate about where one would find X-ray point sources; however, one must run a source detection algorithm in order to determine the locations and physical parameters of the detected X-ray sources. The source detection algorithm is executed by the SAS command, *edetect_chain*; this function is comprised of several individual functions which run and sequence in order to obtain the source data file. The encompassed commands[8], listed in

[8] A detailed description of each of the commands' functions can be found at: "http://xmm-tools.cosmos.esa.int/external/sas/current/doc/edetect_chain/edetect_chain.html".

the order they are run are as follows: *eexpmap, emask, eboxdetect (local), esplinemap, eboxdetect (map), emldetect, esensmap.*

Following the detection algorithm for each camera, the source lists were cross-examined to determine if the same source was detected by multiple cameras; this was done for each observation. In order for a source to be considered for further analysis, it must have been detected on at least two of the three cameras. All of the cross-examinations of the source lists were performed using a program written in python which hereafter will be referred to as *SourceMatch.py.* After which, the source lists were cross-examined across the different observations. From this, we can identify if a source shows X-ray variability. The sources were assigned numbers according to the order they were detected, beginning with observation 1 and ending with 4.

The locations of the detected sources in each observation were exported in RADEC format to region files by *SourceMatch.py*. These region files allow the locations of the sources to be overlaid onto the RGB images, as shown in Figure 10 through Figure 13.

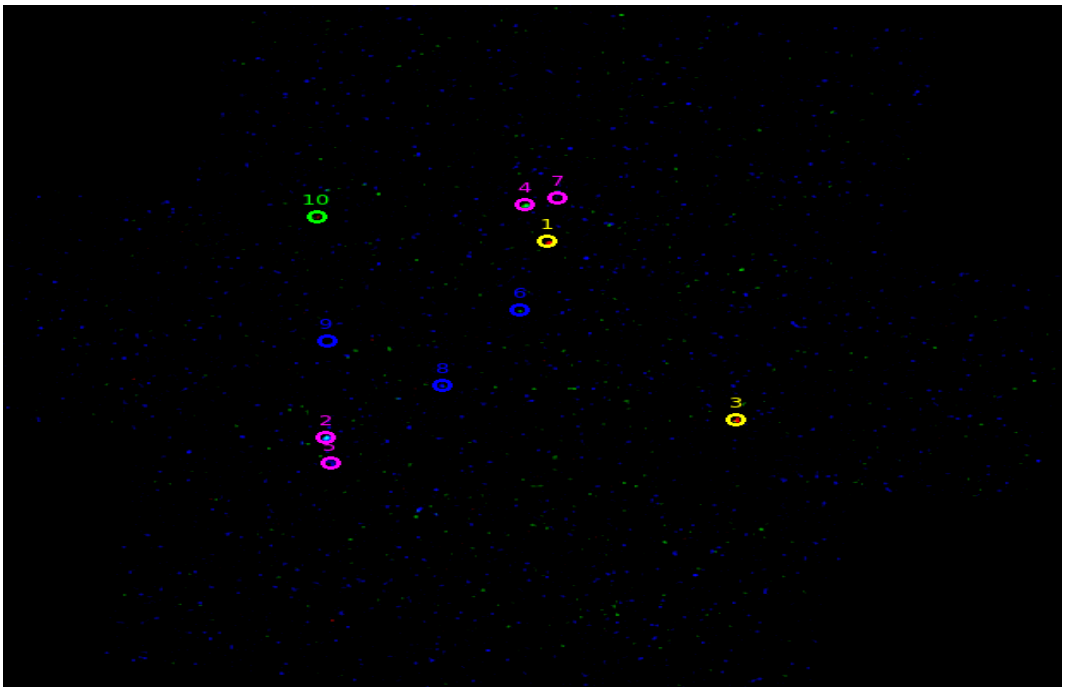

Figure 10: RGB image for MOS2 in observation 1 overlaid with the detected source regions. Colors of the regions indicate the cameras which had a detection likelihood > 10. Yellow = PN, MOS1, MOS2, Red = PN, MOS1, Magenta = PN, MOS2, Blue = MOS1, and Green = MOS2.

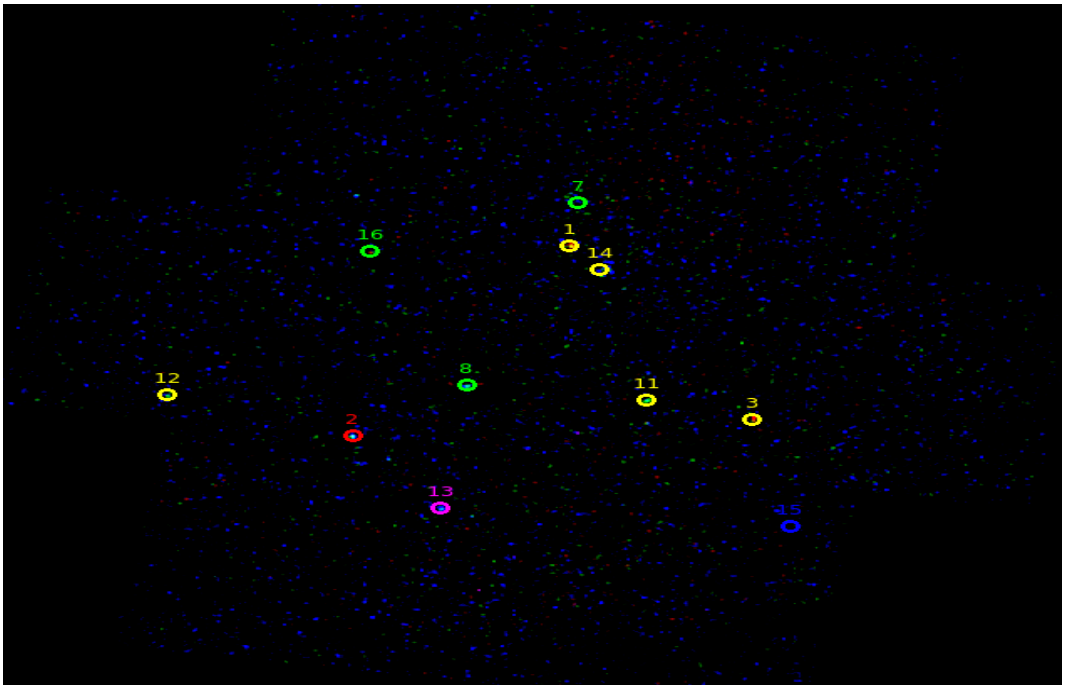

Figure 11: RGB image for MOS2 in observation 2 overlaid with the detected source regions. Colors of the regions indicate the cameras which had a detection likelihood > 10. Yellow = PN, MOS1, MOS2, Red = PN, MOS1, Magenta = PN, MOS2, Blue = MOS1, and Green = MOS2.

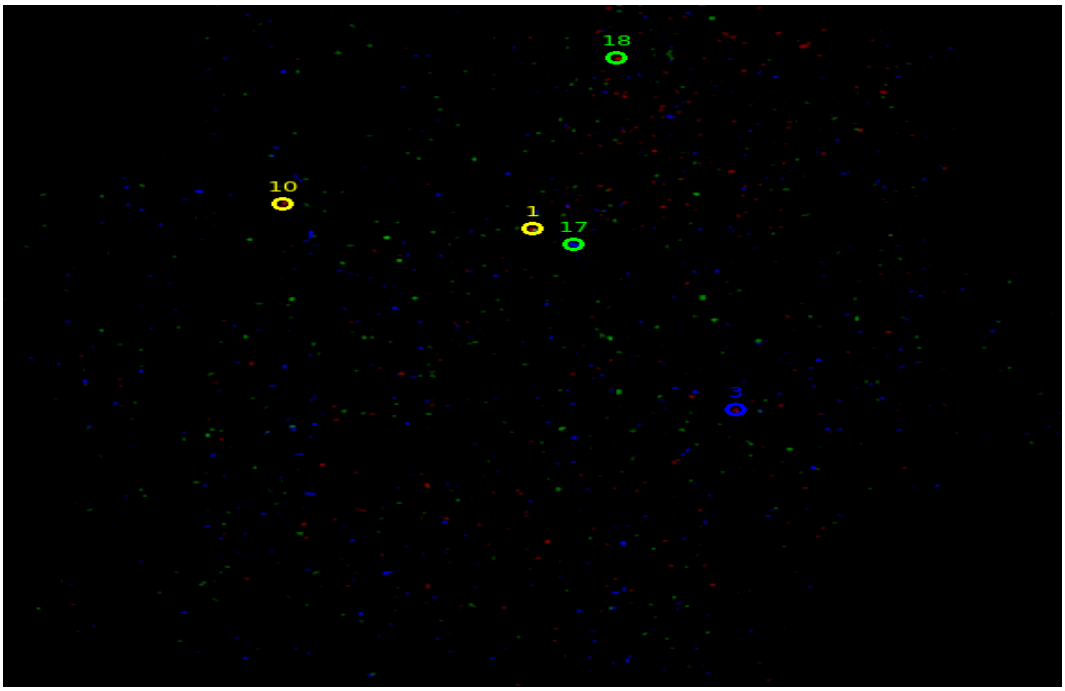

Figure 12: RGB image for MOS2 in observation 3 overlaid with the detected source regions. Colors of the regions indicate the cameras which had a detection likelihood > 10. Yellow = PN, MOS1, MOS2, Red = PN, MOS1, Magenta = PN, MOS2, Blue = MOS1, and Green = MOS2.

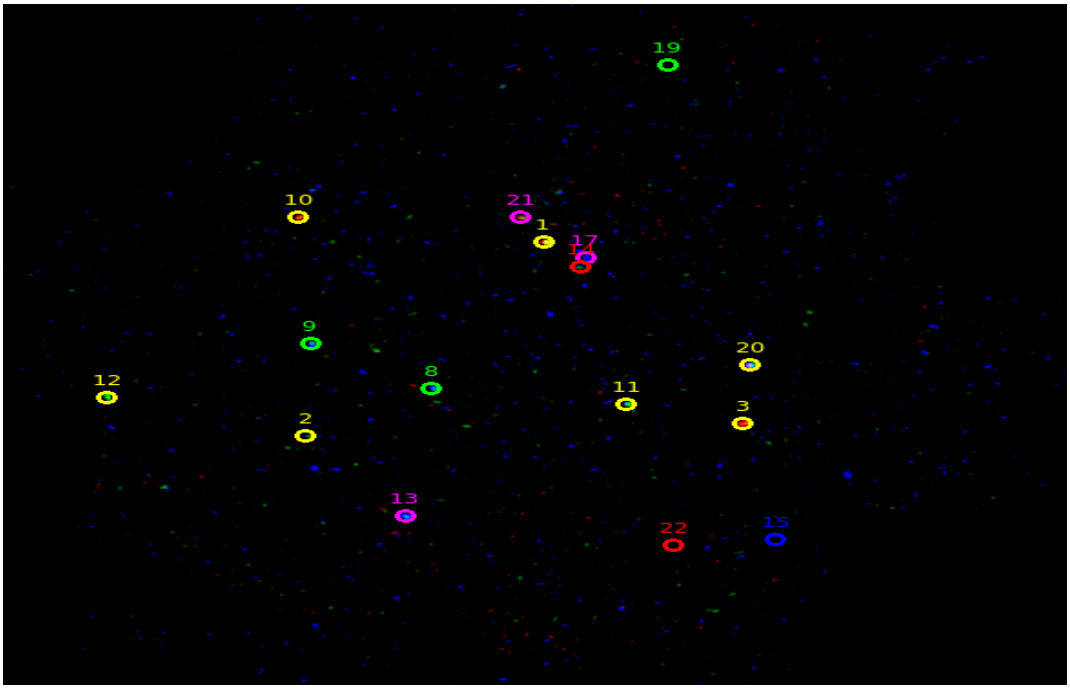

Figure 13: RGB image for MOS2 in observation 2 overlaid with the detected source regions. Colors of the regions indicate the cameras which had a detection likelihood > 10. Yellow = PN, MOS1, MOS2, Red = PN, MOS1, Magenta = PN, MOS2, Blue = MOS1, and Green = MOS2.

2.4 Multi-Observation Light Curves of Suspected Sources

To assist in determining if the detected sources show variability, light curves were compiled across the four observations (Appendix C). Included in these light curves are the count upper limits for sources that were detected in a given observation but were not detected in another. The generation of these light curves also assist in the source selection process for future spectral analysis. Ideally one would aim to first analyze sources that appear most frequently across the four observations, followed by the highest count sources that appear in only one or two observations.

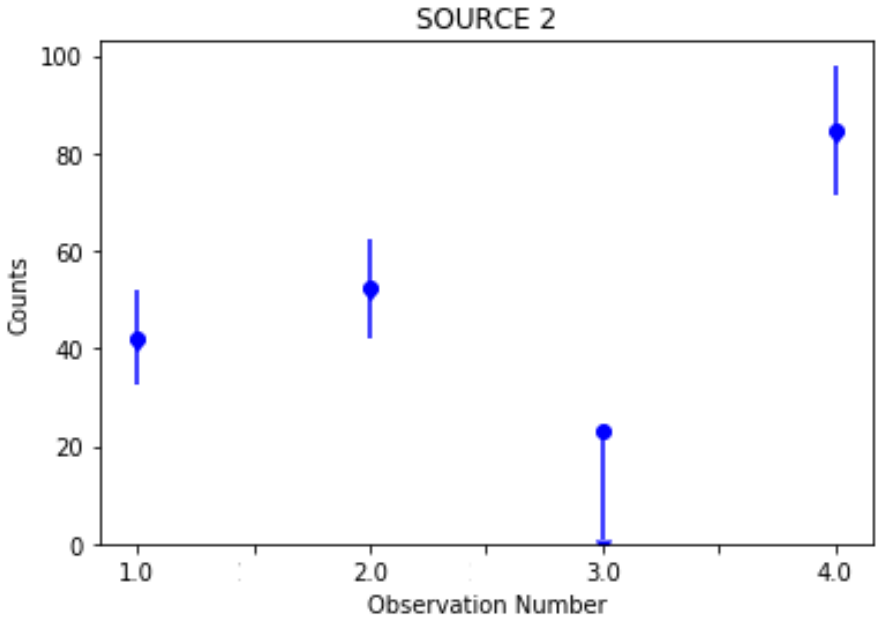

Figure 14: Light curve showing the total counts and their respective errors for source 2 across the 4 observations. Notice in the third observation the source was not detected; however the upper limit for the count number was calculated and is shown by the arrow.

2.5 Optical/NIR Source Counterparts

The positions of the sources selected for further analysis were first cross-referenced (using Vizier) in catalogues by, 2MASS, and Pan-Starrs 1 to determine if

they have registered optical, mid infrared, or near infrared counterparts. Furthermore, photometric data for the parallaxes was obtained from the Gaia DR2 catalogue (Gaia Collaboration, 2018). Cross-referencing these catalogues assists in the classification of the X-ray sources so that YSOs can be properly identified.

2.5.1 Classifying Sources using Catalogue Data

This section is meant to give insight into the steps required in the source classification process. Diagrams and any extensive analysis will be postponed for CHAPTER 3: Results and Analyses. We begin by recording the 3σ positional error (in arcseconds) for each of the sources given to us by the source detection algorithm. This positional error provides a confidence interval within which we can match our source to the catalogue source.

The catalogue Pan-STARRS release 1 (PS1) Survey - DR1 (Chambers+, 2016) was queried with our sources' fk5 positional list as a table input in order to obtain optical data of possible counterparts. The maximum radius from an input location that the catalogue will display a source for (if available) was selected to be the largest 3σ positional error in input list to show possible counterparts to all of our sources[9]. The desired quantities to be displayed were the photometric data for the g-r-i-z-y optical bands (corresponding to effective wavelengths 4866Å, 6215Å, 7545Å, 8679Å, 9633Å respectively), the measurement's uncertainty for each band, and detection flags to

[9] As shown in Table 2 and 3, a catalogued source's radial location from the queried data point is given so each result can be checked if it lies within our 3σ confidence interval.

ensure that the measurements are reliable. A simple output from the PS1 catalogue is shown in Table 2. Output from the other catalogues appears identical in structure.

Full	_r arcsec	_RAJ2000 "h:m:s"	_DEJ2000 "d:m:s"	gmag mag	e_ mag	rmag mag	e_ mag	imag mag	e_ mag	zmag mag	e_ mag	ymag mag	e_ mag
1	0.969	04 56 05.65866720	+47 20 42.3921840	14.7106	0.0077	14.1303	0.0035	13.8764	0.0016	13.7328	0.0081	13.6273	0.0023

Table 2: Pan-Starrs 1 (optical) catalogue output table for a target position corresponding to source 1. The radial distance from the target is given by r (in arcseconds). The photometric data for the g-r-i-z-y optical bands displays the source's apparent magnitude.

Full	_r arcsec	_RAJ2000 "h:m:s"	_DEJ2000 "d:m:s"	Jmag mag	e_ mag	Hmag mag	e_ mag	Kmag mag	e_ mag
1	1.011	04 56 05.65464	+47 20 42.4716	12.710	0.026	12.277	0.030	12.137	0.020

Table 3: 2MASS (NIR) catalogue output table for a target position corresponding to source 1, displaying J-H-K bands' apparent magnitude.

In the near infrared regime, the 2MASS catalogue was searched in order to obtain the J-H-K magnitudes. The J band covers the 1.0-1.5 micron wavelength range, H band covers 1.5-2.0 microns, and finally the K band covers the 2.0-3.0 micron range. Analogous approaches were taken with the Gaia catalogue data. All of the catalogues' data was summarized into concise tables for each source (see Appendix A).

2.5.1.1 Color-Color Diagrams

The first steps taken in attempting to classify the studied X-ray sources is first to create color-color diagrams from the Pan-Starrs 1 and 2MASS photometric data. We use color-color diagrams to compare a star's apparent magnitude at different wavelengths. Main sequence stars of roughly the same age will follow a common trend line on these color-color diagrams called stellar isochrones[10]. The stellar isochrones displayed in the color-color and color-magnitude diagrams have been calculated 100 My stars with solar

[10] Isochrones calculated using CMD (http://stev.oapd.inaf.it/cgi-bin/cmd).

metallicity content. Also added to the diagrams is the 1 My pre-main sequence stellar isochrone. The stellar isochrones display the absolute magnitude for each band. A contributing factor to the apparent magnitudes is the so-called extinction value. Never in astronomy does one have a clear path to the observed object – there is always some amount of dust and gas which, through absorption and scattering, diminishes the amount of light that reaches the detector. The extinction value corrects the apparent magnitude (for each band) of a star by taking into account the diminished intensity due to obstruction of view.

The color-color diagrams plot the relative apparent magnitudes of different bands, also known as the photometric color indices. For the optical portion of the investigation, *g-r* vs *r-i* were the plotted bands. Similarly, *J-H* vs *H-K* plots were used to study the sources' IR data. Sources are first matched to stellar isochrones (if possible), and then looked at further using color-magnitude diagrams.

2.5.1.2 Color Magnitude Diagrams

When a source is matched to an isochrone in the color-color diagrams, it must then be analyzed using color-magnitude diagrams. These diagrams are created by plotting the apparent magnitude for *B* versus the color index *A-B.* In the optical regime, the color-magnitude diagrams are created by plotting the apparent r band magnitude versus r-i. Analogously in the IR, the apparent H magnitude is plotted against H-K. We wish to plot the same isochrones from the color-color diagrams in the color-magnitude diagrams so to see if the sources are still in agreement with the previously matched isochrone. If agreement occurs, it is ruled out that this source is not a YSO and therefore

is not of great importance in this thesis. In order to translate the color-color isochrones to a color-magnitude diagram, the isochrone's absolute magnitude values must be converted into apparent magnitude – a calculation that requires the source's distance which is computed from the stellar parallax obtained (when possible) from the Gaia catalogue. Given the distance, one can easily convert from absolute to apparent magnitude using:

$$m = M + \left(\frac{1}{5} log\, D - 5\right) + A_v \qquad (3)$$

where *m* and *M* are the apparent and absolute magnitudes respectively, *D* is the distance in parsecs, and A_v is the aforementioned extinction value.

2.5.1.3 $Log(F_X/F_{opt})$ vs Hardness Ratio Plots

A final method of preliminary source analysis is through the use of $Log(F_X/F_{opt})$ vs hardness ratio 3 (HR_3). Here, we plot the logarithm of the X-ray flux minus the log of the optical flux and plot it against HR_3. The hardness ratio is the X-ray equivalent of the photometric color index and is defined as:

$$HR_i = \frac{C_{i+1} - C_i}{C_{i+1} + C_i} \qquad (4)$$

where C_i is the exposure corrected counts for the i^{th} band. The five standard bands used in the hardness ratio analysis are: $B_1 = (0.2 - 0.5), B_2 = (0.5 - 1.0), B_3 = (1.0 - 2.0), B_4 = (2.0 - 4.5), B_5 = (4.5 - 10.0)$ where each interval has units keV. Hence, for HR_3, a value near +1 indicates a much larger portion of X-rays in the 2000-4500 keV range than in the 1000-2000 keV range and is called a hard source.

For main sequence stars, once expects to find a relatively low X-ray to optical flux ratio and to be a soft X-ray source ($HR_3 < 0$). Conversely, YSOs exhibit strong X-ray fluxes which exceed the optical. In addition, one can expect $HR_3 \geq 0$. These differences from MS stars allow any YSOs to be clearly identified and the precise criteria will be given in Chapter 3.

2.6 Spectral Analysis of Brightest X-ray Sources

In order to proceed further with analysis, it is necessary to establish what sources will be examined. For some of the detected sources, the count rate is too low (< 40 counts) to generate a spectral energy distribution that would yield any meaningful information. Fitting these low count spectra with the intended models would prove to be problematic at best, and even still, the statistical significance of the results would be very low. It was determined that if a source was detected with more than 40 counts in the 0.2-10 keV range, spectral modeling would be attempted.

The sources for spectral analysis have been selected and matched (if possible) to catalogued optical/NIR counterparts. The energy range for each of the extracted spectra is 0.2-10 keV. Each selected source will have its MOS 1, MOS 2, and PN spectrum extracted (if applicable) and combined in order to improve count rate and statistics. As previously discussed due to the PN camera being better suited to detect in the hard X-ray regime than the two MOS cameras (much higher quantum efficiency for 6-10 keV), we receive a final spectrum with a balanced detection efficiency across the entire 0.2-10 keV range.

A spectrum of the source is extracted by passing a circular 2-D region into the *evselect* filter expression. This circular region has the x,y source location (in physical coordinates) as its center and has a radius of 300 in the physical coordinate system which corresponds to approximately 15 arcseconds which is the half energy width (HEW) of the XMM-Newton telescopes' point spread function (PSF). While the detection algorithm can locate the source's position for a 3σ uncertainty ∼3", the individual photons arrive over an area described by the PSF. By selecting a region that covers the HEW and efficiently subtracting the background, we obtain the best signal to noise ratio. As mentioned, the final spectral product also requires a spectrum of the background region, which must be close to the source. In order to select a background region near and symmetrical about the source region, an annulus region whose center coincides with the circular source region is used. The inner and outer radii of the annulus is chosen to be 400 (20") and 550 (27.5") units respectively in the physical coordinate system.

Following the creation of a spectrum, the command *backscale* must be run with the newly created spectrum, and the eventlist as inputs. The *backscale* command calculates the area of the selected region used to make the spectral file. The *backscale* calculation can be simply written as: $area = (geometrical\ area) - (ccd\ gaps) - (bad\ pixels)$. This area is then written into the header of the spectral file which is required and read when creating the background-subtracted spectrum for the source.

Once the spectral extraction and are calculations are completed, the so-called redistribution matrix file or RMF must be computed via the command *rmfgen*. This

process reformats the standard CAL detector response for a given camera and corrects for instrumental effects specific to the utilized selection criteria. The output file,

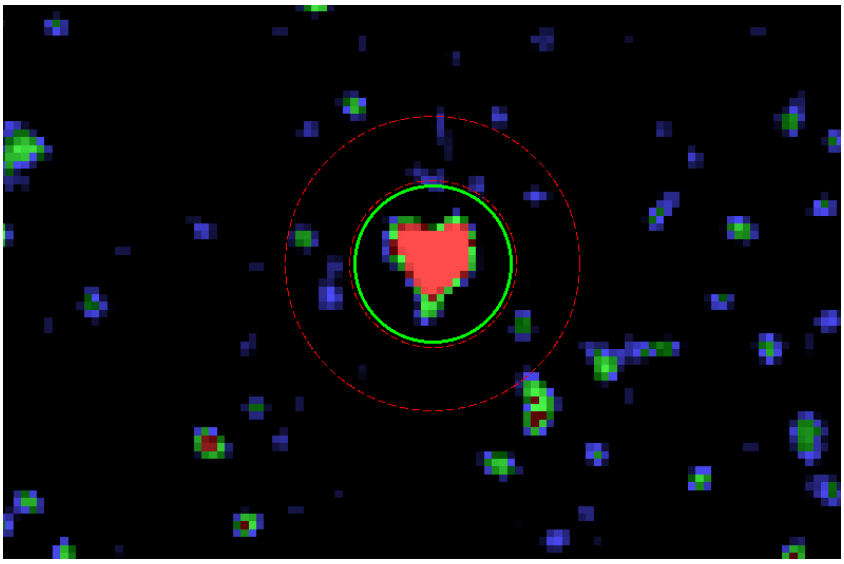

Figure 15: X-ray source circular selection region (green) and background annulus selection region (red). This particular selection region image corresponds to source 20 in observation 4.

describing the instruments response, is written to a .rmf file which will be used later in the spectral-combination of the three XMM-Newton cameras. Finally, *arfgen* is executed and generates an ancillary response file or ARF. The *arfgen* command requires the source spectrum and RMF as input. This file contains area values for a number of different energy ranges and is used in the preparation of the final background-subtracted source spectrum for a single camera.

Given that the source spectrum, background spectrum, RMF, and ARF have been generated, the final background-subtracted spectrum can be created using the command *specgroup*. This command requires the four aforementioned files as input, and from them produces the background-subtracted source spectrum and the

corresponding RMF file. This process is repeated for each camera the particular source was detected on.

Finally, now that a background-subtracted spectrum exists for each camera, the command *epicspeccombine* can be used to combine the three cameras' spectral files into a single spectrum that contains higher counts and thus better statistics.

2.6.1 Model Fitting

In order to extract information from the created spectra the data must be fitted with a model, this allows physical parameters of the source to be read out from the fit parameters if the model is deemed a good fit.

The model used for the sources is a multiplication of the *apec* model (thin plasma thermal emission model) and the *phabs* (photoelectric absorption model. The photoelectric absorption model describes X-rays which are absorbed and reemitted by the hydrogen gas surrounding and along the line of sight of the star. The thermal emission thin plasma model fits an emission spectrum for high temperature (thermal) plasma (>1MK). The obtained parameters from the model fitting are the equivalent hydrogen column density (10^{22}atoms cm^{-2}) and the plasma temperature (keV). If this model cannot be fit to the data due to low statistics, the thermal emission model is replaced with a simpler blackbody model, *bbody*, which retuns an approximation for the plasma temperature in keV.

Using the obtained parameters for a given source, in combination with the optical/NIR catalogue data, the sources can be categorized according to their

evolutionary stage. Furthermore, with photometric data from the Gaia DR2 catalogue (Gaia Collaboration, 2018), we can determine if there are YSOs in the HII forming region and possibly have been influenced by the SNR HB9 shock. The photometric data allows a distance to the object to be determined, and thus we can determine if the object is in the vicinity of the shock knowing that HB9 is located in the range of 2-4 kpc away.

CHAPTER 3: Results and Analyses

In order to distinguish YSO candidates from foreground stars, classification conditions must be formulated. As discussed in previous chapters, the X-ray flux of YSOs (Class I-III) can be orders of magnitude greater than their optical flux; thus, the first classification condition for a foreground star requires $\log\left({F_x}/{F_{opt}}\right) \leq -0.5$. Furthermore, the majority of X-rays produced in main sequence stars are soft, and as a result of this we are able defined the rest of the criterion (adapted from Saeed et al. 2016 [18]) as: $HR_2 \leq 0.0,\ HR_3 \leq -0.5,\ HR_4 \leq -0.5.$

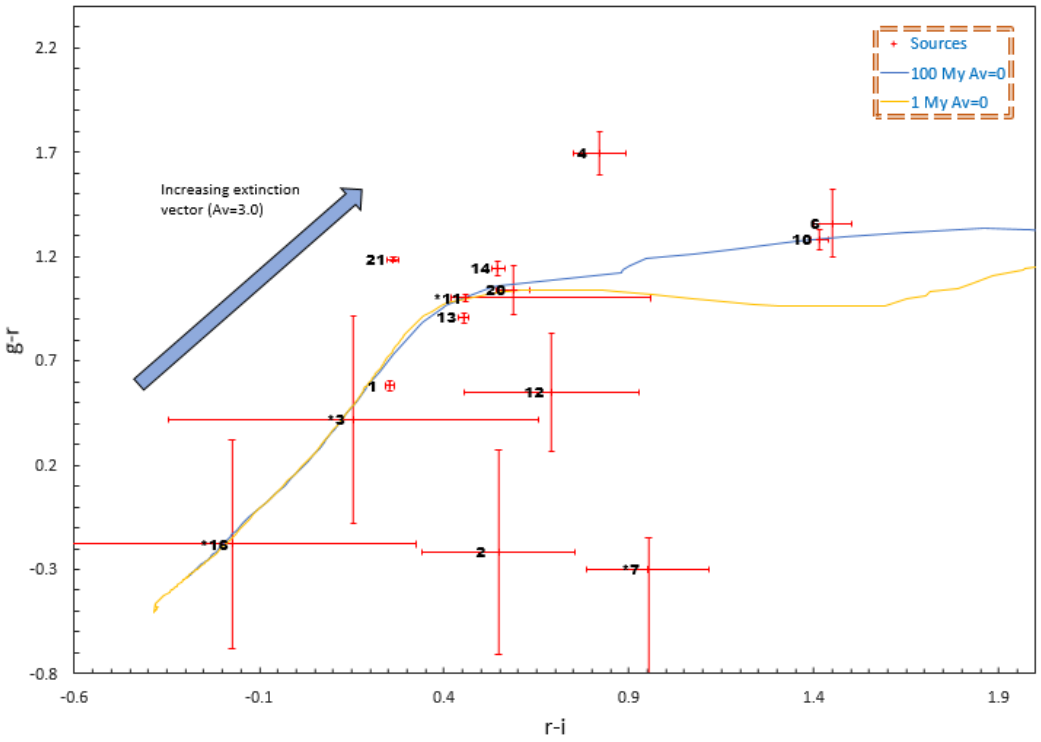

Figure 16: Optical color-color diagram with all sources which had counterpart data in the Panstarrs-1 catalogue. The blue line shows the 100My MS stellar isochrone and the gold line shows the 1MY PMS stellar isochrone, both with zero extinction. Sources marked with an asterisk (*) did not have errors reported for at least one of the photometric bands. See Table 4 for list of band(s) without errors given, also indicated by an asterisk.

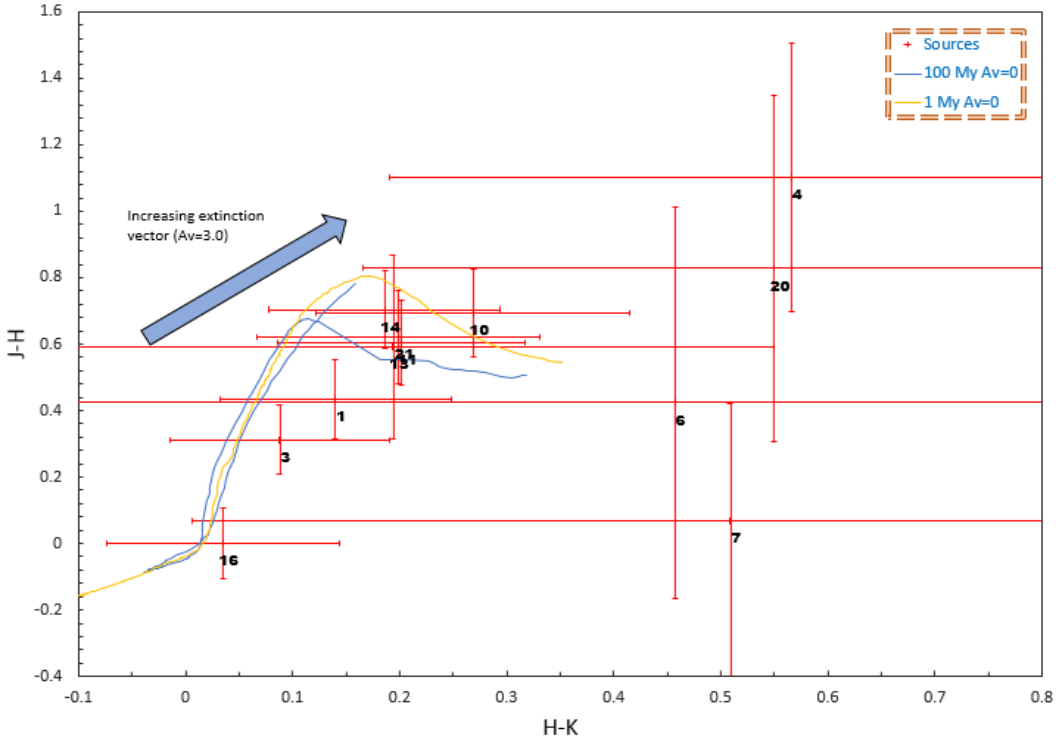

Figure 17: Near infrared color-color diagram with all sources which had counterpart data in 2MASS catalogue. As in the optical diagram, the blue line shows the 100My MS stellar isochrone and the gold line shows the 1MY PMS stellar isochrone, both with zero extinction.

The color-color diagrams for the optical and near infrared show the photometric magnitudes of the sources as well as the main sequence stellar isochrone photometric magnitudes. Due to all YSOs except Class III having thick circumstellar disks, we expect to see infrared excess and to be dominantly red in the optical.

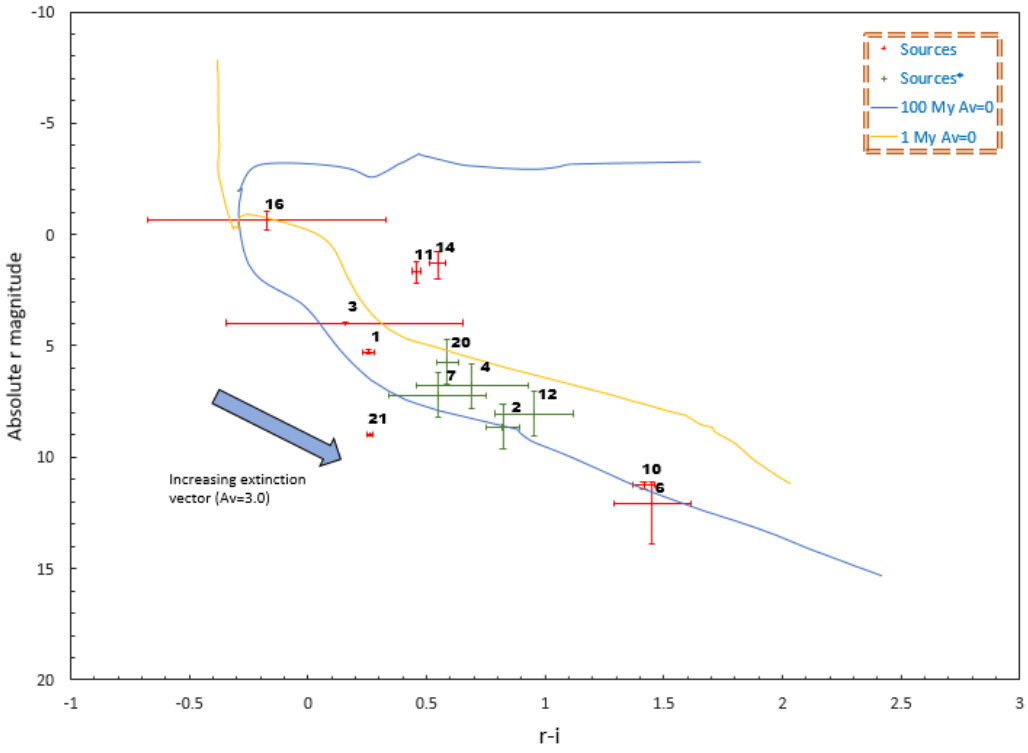

Figure 18: Optical color-magnitude diagram. The sources which had reliable parallax information reported by Gaia are shown in red. Sources of interest that did not have parallax information had their distances estimated to be in the 3.5-4.5 kpc range and are shown in green. The blue line shows the 100My MS stellar isochrone and the gold line shows the 1MY PMS stellar isochrone, both with zero extinction.

In addition to the color-color diagrams, the use of color-magnitude diagrams helps in identifying infrared excess and determining if the star is 'redder' than expected for a main-sequence star. Unfortunately, due to lack of stellar parallaxes from the Gaia catalogue, a good deal of sources', many of which present great interest from their position on the color-color diagrams, could not have their absolute magnitudes precisely determined. In order to remedy this, for sources of interest, specifically source 2, 4, 7, 12, and 20, the distance to the object was estimated to be in the 3.5-4.5 kpc range, which is the HII approximate range and also the estimated influence distance of

the SNR. This estimated distance to the source allows them to be added to the color-magnitude diagram.

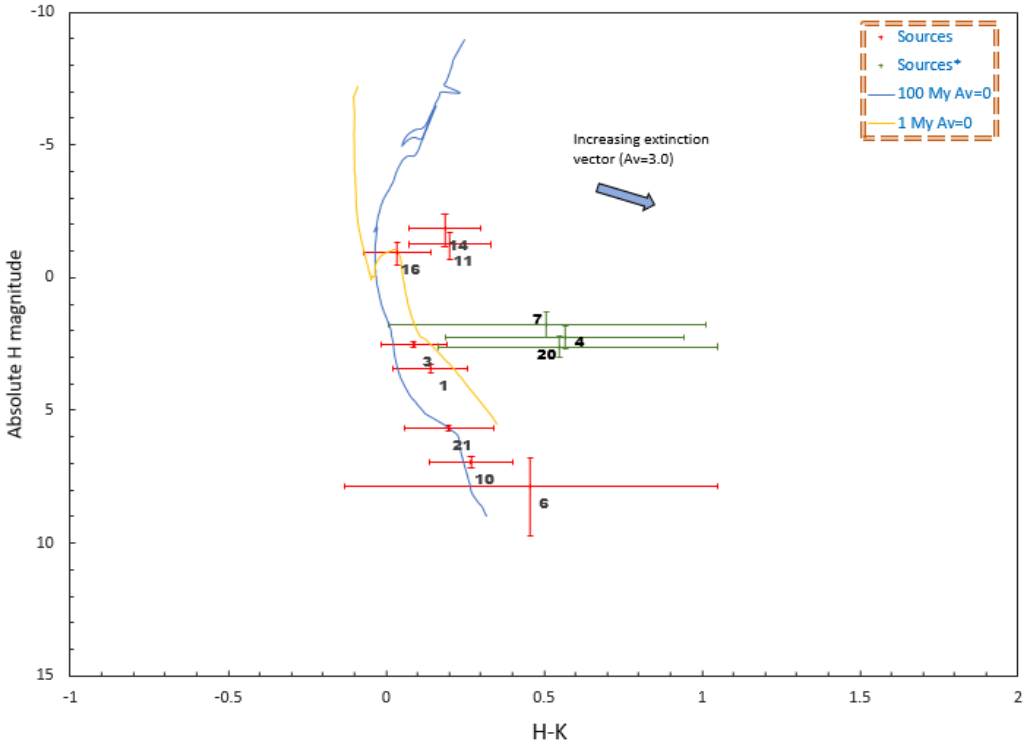

Figure 19: Near infrared color-magnitude diagram. The sources which had reliable parallax information reported by Gaia are shown in red. Sources of interest that did not have parallax information had their distances estimated to be in the 3.5-4.5 kpc range and are shown in green. The blue line shows the 100My MS stellar isochrone and the gold line shows the 1MY PMS stellar isochrone, both with zero extinction.

In addition to the color-color and color-magnitude diagrams, the logarithmic X-ray to optical flux over the 3rd hardness ratio is used to aid in the classification of the sources. The $\log(F_x/F_{opt})$ vs HR_3 plots are displayed separately for each observation. Combination of the observations into one plot is not possible due to the variable nature of YSOs in the X-ray.

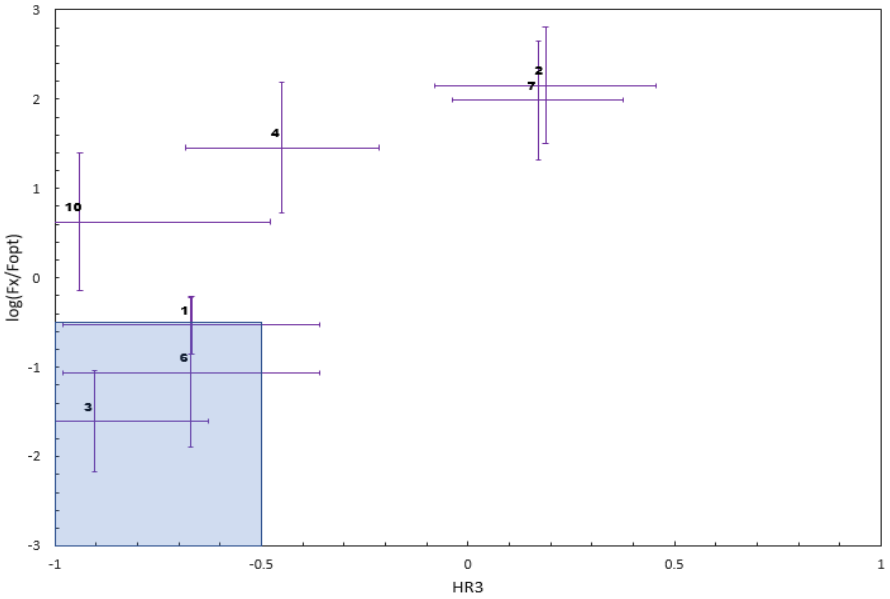

Figure 20: Logarithmic X-ray to optical flux ratio over hardness ratio 3 for observation 1. The blue rectangular region indicates the classification space of a main sequence foreground star.

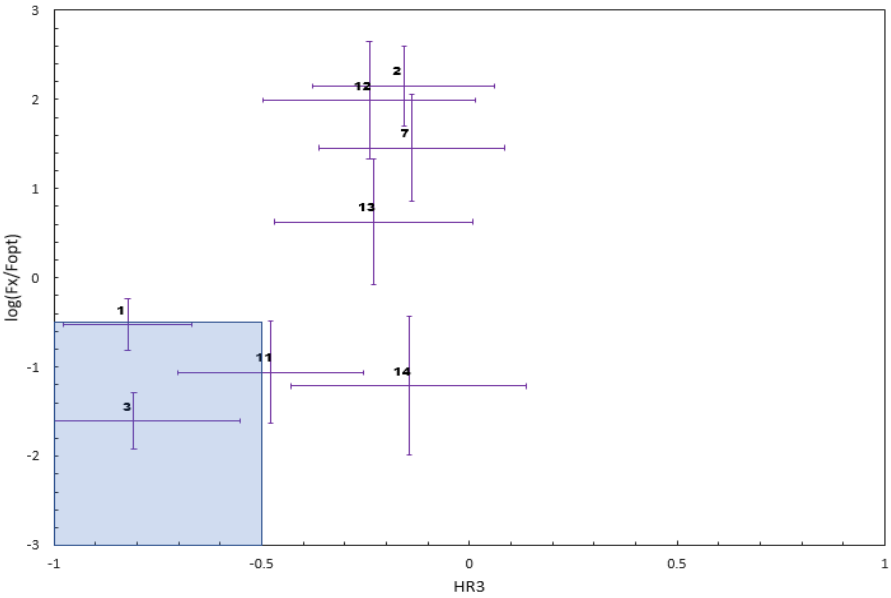

Figure 21: Logarithmic X-ray to optical flux ratio over hardness ratio 3 for observation 2. The blue rectangular region indicates the classification space of a main sequence foreground star.

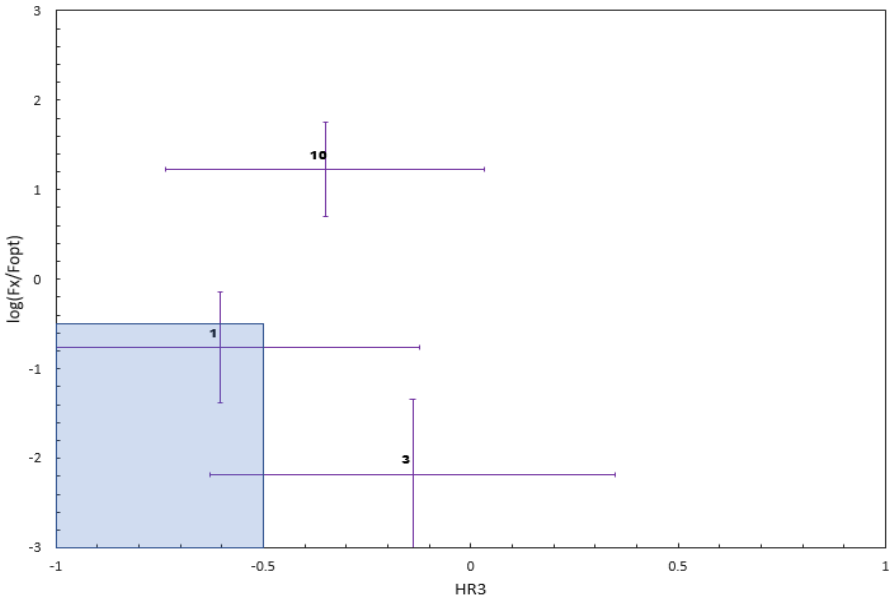

Figure 22: Logarithmic X-ray to optical flux ratio over hardness ratio 3 for observation 3. The blue rectangular region indicates the classification space of a main sequence foreground star.

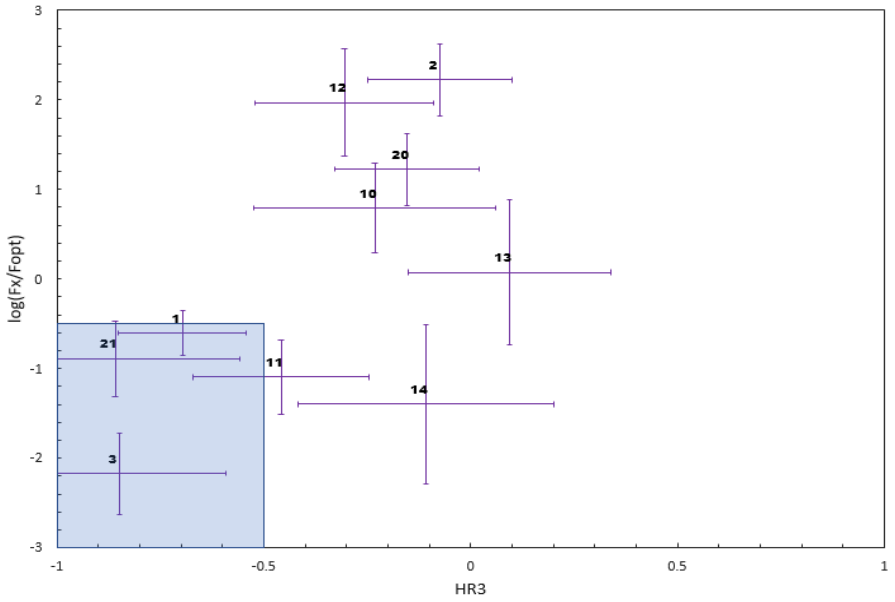

Figure 23: Logarithmic X-ray to optical flux ratio over hardness ratio 3 for observation 4. The blue rectangular region indicates the classification space of a main sequence foreground star.

Hardness ratio vs hardness ratio plots are utilized to analyze sources and determine the dominant energy ranges of the sources. Recall the energy band count formula used to

calculate the hardness ratios from section 2.5.1.3. As previously discussed, main sequence stars are softer X-ray sources than YSOs. The expected hardness ratios for a main sequence star are: $HR_1 > 0, HR_2 \leq 0, HR_3 \leq -0.5, HR_4 \leq -0.5$ and for YSOs we expect to have ratios of: $HR_1 > 0, HR_2 > 0, -0.5 < HR_3 < 0.5, HR_4 \leq 0$. The plots can be found in the appendices.

3.1 Main Sequence Foreground Stars

Since we are only interested in examining star formation and young star development as a possible result of the SNR shock interaction it is important to eliminate those sources indeed X-ray source but are not young stellar objects and instead are X-ray emitting main sequence foreground stars.

Source 1 falls along the stellar isochrone with an interstellar extinction magnitude of 0.9 and corresponding to a MS star of age 100 My with solar metallicity content. Conferring with the JHK color-color diagram we find that source 1 matches to the same stellar isochrone as in the optical. The Gaia photometric data for source 1 locate it at ~590 parsecs, which is not within the HII region, nor the influence region of SNR HB9. This distance was used to compute the apparent magnitudes in optical and NIR and attempt to match them to the same stellar isochrone as in the color-color diagrams. This source falls very near to the extinction-less stellar isochrone and it can be seen from the increasing extinction vector that it coincides with an isochrone with

an extinction value of approximately 0.9, just as in the color-color diagrams. Furthermore, from the analysis of the X-ray to optical logarithmic ratio over HR3, one can see that the source falls within the MS foreground star classification region (blue rectangle). The spectral analysis was performed on this source for observations 1 and 4; however, due to there being a larger number of counts recorded in the fourth observation, we obtain better fitting statistics in this observation and hence a greater confidence in the obtained fit parameters. The temperatures for the plasma surrounding the star were found to be 0.23 keV and the hydrogen column density to be $0.84 \cdot 10^{22}$nH. This plasma temperature is low relative to what one expects for a YSO which further confirms the MS classification from the other analysis tools. The agreement across a platitude of classification means results in source 1 being classified as a MS foreground star.

Source 3 was also classified as a MS foreground star due to the agreement with color-color and color-magnitude diagrams. It should be noted that the Pan-Starrs 1 catalogue only contained the photometric values' upper limits. The source agrees with stellar isochrone when shifted along the extinction vector to a value of 0.9. The distance to the source, used to compute the absolute magnitudes, was reported by Gaia to be 213 parsecs which does not place it within the HII region of interest. Furthermore, conferring with the X-ray/optical flux plot (Figure 20, 21, 23) in observations 1, 2, and 4, it is clear that the source lies within the MS foreground star classification region. In observation 3 the source is still within 3σ uncertainty of the MS region, however this HR_3 value is much larger than in the other three observations. This is due, as previously

discussed, to the large flare periods that needed to be filtered out (GTI filtering) from the observation. There were far fewer counts detected in each energy band, ergo a small count difference between the bands can result in a hardness ratio that differs drastically from the other observations; this also gives rise to the large error that is observed. This flaring period resulting in a larger amount of GTI filtering is also why significantly less sources were detected in this observation than in the other three. Regardless, in observations 1, 2, and 4, the 3σ uncertainty intervals for the flux ratio and HR_3 reside completely within the MS foreground star classification region and therefore we can safely preliminarily classify it as such.

Upon first glance it appears that source 6 agrees with the extinction-less stellar isochrone in the optical color-color diagrams, however one should be aware that the majority of the isochrone values used in producing this curve are found to lie around the steeper-slope portion of the curve. The smaller-slope trailing edge of the curve is formed by approximately 10 points, which pales in comparison to the >200 values that make up the steep portion; as a result, the agreement with this portion of the isochrone should be taken lightly. Moreover, the infrared color indices come with an extremely large uncertainty with hinders the ability to confidently classify this source as a MS foreground star using color-color diagrams. Gaia reports a parallax equating to a distance of 428 pc; however, this measurement came with a large uncertainty. The 99.7% confidence interval for the source's distance is (274 - 985) pc, which does not locate this source within HB9's influence region nor the HII region, Sh2-219. Using this distance interval to calculate the source's absolute magnitude in the r- and H-band, it

can be included in the color-magnitude diagrams, and from them one finds that it is within 3σ agreement of the stellar isochrones in both optical and NIR. The X-ray/optical flux for this source falls within $0.01 < \frac{F_x}{F_{opt}} < 0.62$ and has a hardness ratio $-0.7 < \mathrm{HR}_3 \leq -0.75$. This source was only detected in observation 1 and so only one spectrum is available to model and compare to this classification. The model fit parameters show relatively low plasma temperatures characteristic of main sequence stars and given the results of the other classification tools, this source is placed into the main sequence category.

Source 16 was detected in observation 2 by all three EPIC cameras, although the counts in each were very low (~15 counts per camera). The Gaia parallax reported locates the star at ≈ 820 pc, placing it too near to be located in Sh-219 and to be influenced by the shock front of the SNR. Furthermore, Pan-Starrs 1 had only the photometric upper limits on record, which severely hinders the optical color-color reliability. In both optical and NIR the source is within uncertainty (0.5 upper and lower uncertainty given to optical photometric indices which did not have a reported magnitude uncertainty) of stellar isochrones, and similarly, the source agrees with the extinction-less stellar isochrone in both color-magnitude diagrams. Analysis of the hardness ratio plots indicate that this is a soft X-ray source, locating it in the regions where MS stars exist. Given this, we classify source 16 as a MS foreground star.

Source 21 was located at a distance of 97 parsecs which places it much too near to be influenced by the SNR. The optical measurements do not agree with the stellar

isochrone in the color-color diagram; however, they are within uncertainty of the isochrones in the NIR. Moreover, the color-magnitude diagrams locate the star in close proximity to the isochrones, a small extinction shift of ~0.2 is required in order to reach agreement in both optical and NIR. Inspection of the flux-HR plots show the source being confidently located within the MS foreground star classification box. The spectrum fit parameters yield a plasma temperature of 0.17 keV and a hydrogen column density of $0.71 \cdot 10^{22}$nH, and furthermore the hardness ratio analysis classify this object as a soft X-ray source. As a result, we are able to confidently categorize this source as a MS foreground star.

3.2 YSO Candidates

These sources fit the criterion to be classified as a YSO. To reiterate that criterion, we require: $HR_1 > 0, HR_2 > 0, -0.5 < HR_3 < 0.5, HR_4 \leq 0$ as well as $\log(F_x/F_{opt}) \geq 1$. Furthermore it is expected that the source show reddening in the optical and excess in the NIR. To identify NIR excess the source should be located above and to the right of main sequence stellar isochrones in the NIR color-magnitude diagram. The spectrum fit parameters for these sources should depict a high plasma temperature, with most YSOs having a plasma temperature greater than 0.6 keV [19].

Source 2 presents some difficulties in determining whether it is a YSO candidate or some other X-ray source. The 2MASS catalogue did not have a NIR counterpart recorded for this source and the optical data from Pan-Starrs 1 does not

place the source near a MS stellar isochrone (within 3σ of the photometric uncertainties). Furthermore, there was no stellar parallax recorded in the Gaia catalogue and so its absolute optical magnitude cannot be precisely calculated for use in the color-magnitude diagrams. Instead, the distance to the source was estimated to be in the range of the SNR and HII region, namely in the range 3500-4500 parsecs. This allows us to determine if the source agrees with stellar isochrones if it lies in this distance range. It can be seen that indeed this source does not agree with the isochrones in the optical, showing a greater excess in the blueish g-band. While one would expect a YSO to show reddening in the optical, this bluer appearance can be explained due to commonly observed UV excess in YSOs which arises from the magnetically powered outflow jets. It is possible that this UV excess extends down into the g-band which corresponds to the magnitude in the 400nm-500nm range, which is near the UV cutoff. The necessary information to calculate the source's optical flux is available, and thus it can be included in the $\log(F_x/F_{opt})$ vs HR_3 plots. This source was detected in observations 1, 2, and 4, each of which reported a flux ratio of $F_x/F_{opt} \approx 1000$ indicating that X-ray flux dominates the optical. Moreover, the HR_3 values were measured to be ≈ -0.1 during observations 2 and 4 and ≈ 0.2 during observation 1. Examination of the HR-HR plots indicate that this source is a harder X-ray source than a MS star. It is clear at this time that source 2 is not a MS foreground star, however, it is not certain that it is a YSO. The spectrum was modeled with the *phabs*apec* model for both solar (1.0) metallicity and 0.3 metallicity abundances. The best fit model is obtained when the metallicity abundance was set to 0.3, a common value for modeling YSOs; however, the difference

in the reduced chi-squared value is not very significant (0.993 vs 0.988). Nevertheless, the 0.3 metallicity model is used for the parameter determination. Modeling of the source's spectra returned a plasma temperature of 0.85 ± 0.15 keV and a hydrogen column density of $1.37 \cdot 10^{22}$ nH. The large value for the hydrogen column density is indicative of a thick hydrogen envelope surrounding the object, a feature of YSOs. Furthermore, the high plasma temperature is well above that of a typical MS star and is characteristic of that of a YSO. As a result, this source is classified as a YSO candidate.

There was are no recorded counterpart for source 5 in the optical or infrared regime and this source did not have a stellar parallax recorded by Gaia. The hardness ratio analysis indicate that this source is harder than main sequence stars which raises interest. The count rate was too low to model this source's spectrum with the typical *phabs*apec* model, so in order to obtain an approximation for the plasma temperature, a black body model was used, multiplied with the *phabs* absorption model. The temperature fit parameter was found to be ≈ 1.34 keV, which is a larger temperature than one would expect from the optically thin plasma surrounding a main sequence star. This source is tentatively classified as a YSO candidate. Deeper surveys of this source are necessary in order to confirm/deny the candidacy as a YSO.

Source 7 is one of particular interest because it's right ascension and declination coordinates place it within the HII region, however we do not have parallax information to determine if the star is actually within the HII region or if it is in the foreground or background. In addition to its location in the sky, the source also shows YSO-like properties in its position on the color-color diagrams. We see that in the optical color-

color diagram, the source does not agree with the stellar isochrones - it is far bluer than a main sequence star, placing it below and to the right of the main sequence isochrones. Similarly, to source number 2, the cause for this bluer appearance is due to the UV excess caused by the outflow jets observed in YSOs extending down into the g-band. It must be stated that the catalogues did not report errors for g-band and J-band magnitude, giving rise to the large uncertainty seen in the optical and NIR color-color diagram. Moreover, the H- and K-band magnitudes report large uncertainties resulting in $(H-K)_{error} \cong 0.5$. The hardness ratio plots indicate that this is a harder X-ray source than a MS star. The count rate is too low to model the spectrum and obtain useful statistics. A straight line along the x-axis yields a reduced chi-squared of near 1 which indicates that the signal to error ratio is very low. However, we did find that by applying model parameters obtained from the fit of a MS star, the model does not capture many of the high energy features, indicating that the plasma temperature is larger than the MS model temperature. A high plasma temperature is a characteristic of (but not limited to) YSOs. Deeper studies of this source are necessary to determine its physical properties and evolutionary timeline.

There is no optical, NIR, or parallax information available for source number 9. The RADEC coordinates place this source outside of the Sh2-219, but if the distance in in the 3.5-4.5 kpc range, it would be in the influence region of the HB9 shockwave which has the potential to affect the stellar evolution process. The source was detected in observations 1 and 4; however, the count rate in observation 1 is too low to perform hardness ratio analysis. Observation 4 provides nearly twice the number of counts as

the 1st and as a result it can be seen that the hardness ratio uncertainties are much smaller. The hardness ratios show that this source is harder than a main sequence star. The hardness ratios and uncertainties lie completely within the YSO classification region. Spectral fitting for the 4th observation returned a plasma temperature of 1.08 keV and a hydrogen column density of $2.52 \cdot 10^{22}$ nH. This large nH value is commonly observed in YSOs of Class I/II and II. This source is classified as a YSO, however further studies are recommended.

Source 12 has no NIR counterpart recorded, nor does it have parallax information available from Gaia. This source is found below the optical stellar isochrone, similar to source 7, which tells us that it is redder than one would except a MS star. The distance to the object was estimated to be in the range of 3.5-4.5 kpc, placing it in the influence region of HB9. The flux-HR plots, show that the source is a far stronger emitter in the X-ray than in the optical by a factor of ≈1000. This is surely not a characteristic quality of MS stars and so it remains as a possible YSO candidate. The hardness ratio plots identify this object as a harder X-ray source with $HR_1 \approx 0.64, HR_2 \approx 0.72, HR_3 \approx -0.27, HR_4 \approx -0.90$. Spectral modeling of this source for observation 2 was performed using two metallicity abundance ratios of 1.0 and 0.3. There is no significant change in the reduced chi-squared when changing this parameter, however the sensitivity of the temperature parameter is greatly affected. The 0.3 abundance results in a finer-tuning of the temperature, showing a much smaller range for the 1σ upper-bound. Moreover, we also receive a smaller 1σ interval for the hydrogen column density parameter. Thus, the 0.3 abundance values will be used for

the discussion. The temperature fit parameter of 1.56 keV along with the hydrogen column density of $0.54 \cdot 10^{22}$ nH is indicate of a Class II/III YSO in which the circumstellar disk has become thin.

Optical and NIR counterparts were available for source 13, and their photometric indices place within uncertainty limits of the stellar isochrone of extinction ~2.4, specifically in the optical color-color diagram. The NIR photometric indices contain uncertainties an order of magnitude larger than the optical and so the reliability of the optical color-color diagram is weighted more heavily. The parallax information reported by Gaia is unusable (0.0401 ± 0.3017 mili-arcseconds) and as a result the absolute magnitudes cannot be accurately computed. Instead the distance is estimated to be 3.5-4.5 kpc so that this source can be theorized to be in the influence region of HB9 and included in the color-magnitude diagrams. The RADEC coordinates do not place it near the HII region, but would have been affected by the passing SNR shock should the source's actual distance be similar to that of which it was assigned. The flux-HR plots suggest that the source's optical flux is weaker than that in the X-ray regime, with a flux ratio residing in the 3σ interval of $0.5 \leq \frac{F_x}{F_{opt}} \leq 55$. While the lower limit does not suggest a domination by the X-ray, it is still above the MS classification region. Hardness ratio analysis, based on the classification criterion of Saeed et al. [18], classifies this source as not being a MS foreground star. The large HR_2 values in both observations indicate that this source is a harder X-ray emitter, an expected property of YSOs; henceforth, this source is tentatively classified as a YSO candidate. The spectra did not yield enough statistics in order to fit it with a model.

The optical photometric indices source number 20 place it well within 3σ of the stellar isochrone. The same is true for the NIR color-color diagram, albeit a less reliable measurement due to the 2MASS catalogue only containing the upper limits for the magnitudes (an index error of 0.5 was assigned to J-H and H-K). There was no parallax information available, however the distance was estimated to be in the 3.5-4.5 kpc range so that it could be included in the color-magnitude diagrams. Although the coordinates do not place this source within Sh2-219, having it lie within this range would place near the approximated area of influence of the HB9 shock front. Examination of the flux-HR plot indicates that the source is a stronger emitter in the X-ray than in the optical with a ratio $\frac{F_x}{F_{opt}} \approx 20$. Furthermore, the HR_3 was measured to be -0.15 ± 0.17. The value $HR_2 = 0.36 \pm 0.19$ indicates that this source is harder X-ray source. The spectrum was modeled with a metallicity abundance of 0.3, and the fit returned a temperature of ~ 5.9 keV with a hydrogen column density of $0.17 \cdot 10^{22} \mathrm{nH}$. The goodness of fit had a value of $\chi^2/\mathrm{ndof} = 45.80/39$ which is very acceptable given the available counts. The plasma temperature is far too high to belong to a MS star, and is more-so characteristic of a Class 0/I early stage YSO. These features are not certainly not characteristic of a MS star and so this source remains as a YSO candidate.

3.3 Unclassified/Binary System X-Ray Sources

The optical color-color diagram for source 4 shows it to be dominating in the blue with photometric index values $g - r \cong 1.70,\ r - i \cong 0.82$. One can see that for a large extinction value of ~3, the source is within 3σ uncertainty of the stellar isochrone. Similarly, for the NIR color-color diagram, the source is in agreement (within uncertainty) the stellar isochrone with an extinction value of 3. The NIR photometric errors are large which results in the uncertainty intervals of the source covering a wide area on the diagram and in fact the source's true color indices may not agree with the isochrone's values. The distance was estimated to be 3.5-4.5 kpc and the source's absolute magnitudes were computed for the color-magnitude diagrams. These diagrams showed reddening and NIR excess which is expected for a YSO. The optical/X-ray flux ratio vs HR_3 plot for observation 1, which was the only observation it was detected in, shows the source's flux as being dominated by X-ray, with a flux ratio of $6 \leq \frac{F_x}{F_{opt}} \leq 160$ which corresponds to a 99.7% confidence interval. This flux ratio along with its hardness ratio interval, $HR_3 = -0.45 \pm 0.23$, places the source just outside the MS foreground star classification region with errors extending into the region. The HR-HR diagrams indicate that this source has a $HR_2 = 0.90 \pm 0.17$ which is much higher than for a MS star. The HR_1 value is unreliable for analysis because of very few counts recorded in energy bands 1 and 2, which results in an enormous error (> 2). We also obtain a value of $HR_4 = -0.33 \pm 0.50$ which has errors extending into the non-YSO classification region of $HR_4 > 0$. While we can classify this source as not being a MS

star due to the high X-ray/optical flux and hardness, its classification as a YSO is tentative; deeper studies are required to confidently classify this source. The majority of the counts for this source were found in the 3rd energy band (1-2) keV. Spectral analysis cannot be performed due to the number of counts being far too low to obtain useful statistics from the model. Hence, physical parameters for the object cannot be determined.

Source 8 does not have g- and r-band magnitudes available within the Pan-Starrs 1 catalogue. Furthermore, this source has no recorded NIR counterpart, nor did the Gaia catalogue have a parallax recorded. As a result, we cannot add this source to the color-color, color-magnitude, or flux ratio vs HR_3 plots. Analysis of the hardness ratios during observation one do not provide any classification insight due to the large errors - a consequence of the low counts. Observations 2 and 4 reported higher counts and smaller hardness ratio uncertainties; however, the two observations do not fine common ground on a value for HR_2 with observation 2 having reported $HR_2 = 0.90 \pm 0.40$ and observation 4 reporting $HR_2 = -0.10 \pm 0.39$. The 3rd hardness ratios also varied between observations with $HR_3 = -0.45 \pm 0.31$ and $HR_3 = -0.06 \pm 0.41$ in observations 2 and 4, respectively. The spectrum did not provide enough statistics to be accurately modeled with *phabs*apec*. The fit was tried for 1.0 and 0.3 solar metallicity abundances and in both cases was completely insensitive to the hydrogen column density parameter. The temperature fit parameter was most sensitive for the 0.3 metallicity fit and was found to be 2.49 keV and have a 1σ range of $(1.61, 5.09)$ keV. The low counts coupled with large errors on the background subtracted binning results

in this fit being unreliable in the source categorization process and so this source cannot be classified.

Source 10 displayed extremely large optical color indices ($g - r \approx 1.3,\ r - i \approx 1.4$). Gaia reported a parallax corresponding to a distance of ≈200 pc which places the source far too near to be affected by the SNR; however, the measurement uncertainty was approximately 10% and so the reliability of this measurement and thus the reliability of the color-magnitude diagrams can be questioned. Source 10 matches with the trailing edges of the stellar isochrones for the optical and NIR color-color diagrams, but as previously mentioned, agreement with this portion of the isochrone does not carry significant weight. From the color-magnitude diagrams we find that there is agreement within 3σ for the extinction-less isochrone in the optical color-magnitude diagram, but to obtain agreement in the NIR, one must shift the isochrone along its increasing extinction vector. We find some common ground around an extinction value of approximately 0.3. Moreover, we notice that the X-ray to optical ratio is $\frac{F_x}{F_{opt}} \approx 10$ for the three observations (1,3, and 4) that it is observed in and henceforth, we cannot categorize this source as a MS foreground star. The 2nd hardness ratios for this source indicate that it is a softer X-ray source in the 2nd and 3rd energy bands, however HR_3 does not categorize it as being as soft of source as a MS star. The conflict in YSO and MS criteria indicate that this source is neither a MS foreground star nor a YSO. Due to the large apparent magnitudes in the optical and NIR, it is clear that this is faint source

in the optical and NIR. Source 10 is classified as a low mass X-ray binary system (LMXB).

Source 11 is of particular interest due to Gaia reporting its distance to be ~2.7 kpc places it within the estimated influence region of SNR HB9; however, its distance does not place it within that of the HII region. The source agrees with the color-color and color-magnitude stellar isochrones (shifted along the increasing extinction vector) in both the optical and NIR regime. One finds that in order to obtain agreement within the color-magnitude diagrams, a large extinction value is required. This is logical due to the source being located at a large distance, which increases the likelihood of their being a larger amount of interstellar gasses between the source and the observing instrument. The source was detected in observations 2 and 4. Referring to the X-ray/optical flux vs HR_3 plots, it can be seen that the source is within uncertainty limits of the MS region. However the HR_2 The flux ratio during the two observations is $\frac{F_x}{F_{opt}} \approx$ 0.1 which states that the optical regime dominates the X-ray, a trait that is not true for YSOs. In both observations the flux ratio's uncertainties reside completely within the MS classification requirements, and it can be seen that in observation 4 where approximately 25% more counts for this source (91 in obs. 2 and 120 in obs. 3) were recorded, the HR_3 value was in more agreement with the MS star region. Given this information, source 11 could be classified as a main sequence star; however, we find that $HR_2 = 0.55 \pm 0.23$ in observation 2 and $HR_2 = 0.38 \pm 0.21$ in observation 4, making it too hard in these energy bands to be classified as a MS star. Confident classification of this x-ray source cannot be made at this point.

Source 14 appears very similar to source 11 in its color-color, color-magnitude, and flux-HR plots. The parallax information for this source places it in the range of 2.6 kpc – 4.6 kpc and so it is possible that it is in the influence area of the HB9, although the RADEC coordinates place it outside the HII region of interest. This is a harder X-ray source than a main sequence star, with the hardness ratios placing it in precisely in the regions that YSOs would live. However, we find that the X-ray to optical flux ratio is $\frac{F_x}{F_{opt}} \approx 5 \cdot 10^{-2}$ which is not characteristic of YSOs. This source agrees with stellar isochrones when shifted to a large extinction value, due to the great distance to the source. This source does not meet the criterion [18] to be classified as a MS star, however it is tentatively ruled out as a possible YSO candidate due to the X-ray flux being two orders of magnitude smaller than the optical. The extracted spectrum from the fourth observation was modeled and returned a plasma temperature of ≈ 1.08 keV and hydrogen column density of $0.89 \cdot 10^{22}$ nH. Additional observational data is required in order to properly classify this source.

Source 17, much like source 14 is located on the outskirts of the HII region of interest. There is no photometric data. The entirety of the counts (except for 1-5 but this value was less than the count errors in the band) were detected in energy bands 4 and 5 which is the cause for the extremely large error bars for HR_1 and HR_2. Hardness ratio analyses of the upper bands suggest that this is a much harder-than-MS X-ray source. The spectrum for this source in the fourth observation was modeled with *phabs*apec* and retuned a temperature and hydrogen column density values of $\sim 6.6 \cdot$

10^{22}nH and 9.1 keV, respectively for a goodness of fit of $\chi^2/\text{ndof} = 35.67/31$. The low counts and large errors may be the reason why the reduced chi-squared of this model suggests it to be an accurate fit. The 1σ errors on the model parameters are very large, indicating that the fit is fairly insensitive to the parameters. These model results, should they be deemed as accurate representations of the object, indicate that this source has plasma temperatures far exceeding that of a MS star; however, the hydrogen column is much high than expected for a MS star but also much higher than on would expect for a YSO which leaves the validity of this model to be questioned. Deeper studies of this source are necessary in order to determine the nature of this source.

3.4 Non-Sources

No photometric data was available for source 15. More importantly, this source was only detected as an X-ray source on the MOS-1 camera in both observations (2 and 4). The count to error ratio is extremely high (>30%) with most of the counts being $<$ 0.3 keV suggesting that it is soft proton contamination. As a result, the hardness ratios are insignificant to the analysis. This is categorized as a non-source.

Source 18 has no photometric data available. The hardness ratio analysis cannot be taken seriously due to the extremely low count rate. Moreover, for the PN camera, there were no counts detected in energy bands 1, 3, and 4 and the counts that were recorded in the 1st and 5th had ~50% uncertainties. The MOS-2 camera had even fewer counts in total, again with 50% uncertainties. This so-called source is no more than

noise. The location of this source is near the top edge of the MOS-2 F.O.W. There is the possibility for bad pixels in that area which is the same case as the following source, number 19. This is therefore excluded from the analysis and marked as a non-source.

There was no photometric available for detected source number 19. Furthermore, this source was in close proximity of so-called source 18 and was only detected for the MOS-2 camera, very near the edge of the CCD. The count rate error is ~25% of the total counts and the hardness ratios for this source do not categorize it as a MS star or a YSO candidate. Finally, upon examination of the logarithmic scaled spectrum (shown in the appendices), we find that the majority of the 66 counts had energy of ~0.3 keV, typical of soft proton contamination, which results in a $HR_1 \approx 0.76$. The other energy bins indicate that this detected source is no more than noise, with the background subtracted spectrum showing negative counts for some bins and very few positive counts for other bins. This detected source is therefore excluded from the analysis and categorized as a non-source.

No photometric data is available for source 22, but more importantly, the spectrum revealed that ~99% of the counts is due to soft proton contamination $(< 0.3 \text{ keV})$ and thus can be excluded from further discussion and classified as a non-source.

CHAPTER 4: Discussion

The observations which studied the shock front region of HB9 and included the Sh2-219 HII region did not yield a significant amount of YSO candidates within the HII region, and those sources that were classified as a potential candidate lacked the number of counts required to produce meaningful statistics in the spectral analysis. The optical, NIR, and parallax information served to eliminate a great deal of sources from the list of potential candidates.

The sources of particular interest, having coordinates coinciding with Sh2-219, were 1, 4, 7, 14, 17, and 21. Sources 1 and 21 were confidently ruled out as YSO candidates and were classified as foreground main sequence stars. Source 1 appears to lie in the RADEC coordinate location of the HII region and appeared predominately red in the r-g-b XMM-Newton images created for each observation. However, the source had optical and NIR counter parts which located it along the 100My main sequence stellar isochrones. Furthermore, the parallax data from Gaia locates this source much too near to be within Sh2-219 or to be within the affected regions of HB9. The aforementioned information alongside the hardness ratio and spectral analysis indicate that it is a foreground star. Source 21 shared many of the same features as source 1, having softer X-rays, a low X-ray/optical flux ratio, and a plasma temperature of 0.17 keV. Sources 4, 14, and 17 all appear to be in close proximity to the HII region, however they lacked sufficient data to make confident classifications. Source 4 shows a high X-ray/optical flux, eliminating the possibility of it being main sequence. It was

not in close agreement with the stellar isochrones for the color-color diagram, but it could be due to strong extinction. The color-magnitude diagrams did not show agreement with the isochrones when the objects distance was estimated to be in the 3.5-4.5 kpc range. Moreover, the hardness ratios indicate that this source is softer than expected for a YSO. Spectral analysis could not provide insight into the nature of this object due to low count rates. Source 7 was of great interest, with its coordinates locating it within Sh2-219. Unfortunately, Gaia did not have a stellar parallax for this source on record, but the distance was estimated to be that of the HII region in order to place the source on the color-magnitude diagrams. The photometric data show that this source is well below the stellar isochrone, appearing much redder than a main sequence star. This is expected of a YSO due to their thick envelopes absorbing and reemitting light at longer wavelengths. The spectrum of this source could not be fit with the thermal plasma model due to the counts being low, thus resulting in low fitting statistics. Parameters for known MS stars, namely source 1 and 21, were used in the model for source 7 in order to get a qualitative goodness of fit. The MS model overlaying source 7's spectrum indicated that the model did not capture the high energy X-rays which is what one should expect if source 7 is indeed a YSO. Hardness ratio analysis indicate that this source is much harder than a MS star and falls within the HR regions where one would find YSOs. Deeper studies of this source are needed in order to determine if this is a YSO and if its formation was triggered by the shock front of HB9 or if its stellar evolution is impacted by the shock front due to the heavy metal deposition and increased plasma temperatures that comes along with the SNR interaction.

Sources 2, 5, 9, 12, 13, and 20 were classified as YSOs, however their RADEC coordinates do not place them within the HII region. Further studies of these sources are valuable nonetheless in order to gain insight into the interaction of pre-existing YSOs with SNR shock fronts. The heavy metal content that SNRs bring with them could significantly alter the stellar evolution of the YSOs, sending it on a different evolutionary track. In addition, the heating of a YSO's circumstellar gas due to the shock wave could have evolutionary implications.

There were a handful of sources which lacked sufficient data and therefore could not be properly classified. The hardness ratios for these sources (4, 8, 10, 11, 14, and 17) excluded them from classification as a main sequence foreground star, however some of these sources did not show high X-ray/optical flux ratios and/or had spectra with too low statistics to be confidently modeled. It is hypothesized that some of these sources could be LMXBs while others may be some other type of X-ray emitting compact object. Deeper studies of these source are required for accurate classification and examination of the shock-source interaction.

References

[1] M. Barsony, "Class 0 Protostars," *Astronomical Society of the Pacific* , vol. 65, pp. 197-206, 1994.

[2] T. Preibisch, "XMM-Newton study of the Serpens star-forming region," *Astronomy & Astrophysics,* vol. 410, pp. 951-959, 2003.

[3] M. Jardine, A. Cameron, J.-F. Donati, S. Gregory and K. Wood, "X-ray emission from T Tauri stars," *Royal Astronomical Society,* no. 367, pp. 917-927, 2005.

[4] B. Reipurth and J. Bally, "Herbig-Haro Flows: Probes of Early Stellar Evolution," *Annual Review of Astronomy and Astrophysics,* vol. 39, pp. 403-455, 2001.

[5] R. E. Pudritz, R. Ouyed, C. Fendt and A. Brandenburg, "Disk Winds, Jets, and Outflows: Theoretical and Computational Foundations," in *Protostars and Planets V*, University of Arizona Press, 2007, pp. 277-295.

[6] B. Stelzer, "X-ray variability of cool stars: Magnetic activity and accretion," *Astronomische Nachrichten,* vol. 338, no. 2-3, pp. 195-200, 2017.

[7] B. Stelzer and R. Neuhäuser, "X-ray emission from young stars in Taurus-Auriga-Perseus: Luminosity functions and the rotation -activity -age -relation*," *Astronomy & Astrophysics* , vol. 377, no. 2, pp. 538-556, 2001.

[8] A. P. Goodson and R. M. Winglee, "Jets from Accreting Magnetic Young Stellar Objects. II. Mechanism Physics," *The Astrophysical Journal,* vol. 524, no. 1, pp. 159-168, 1999.

[9] M. Guedel and Y. Naze, "X-Ray Spectrroscopy of Stars," *Astronomy & Astrophysics,* vol. 17, no. 3, p. 341, 2009.

[10] P. Höflich and J. Stein, "On the Theromonuclear Runaway in Type Ia Supernovae: How to Run Away?," *The Astrophysical Journal,* no. 568, pp. 779-790, 2002.

[11] D. Sugimoto and K. Nomoto, "Presupernova models and supernovae," *Space Science Review* , vol. 25, no. 2, pp. 155-227, 1980.

[12] K. Throne, The Particle Kinetics of Plasma, 2012.

[13] H. C. Connolly Jr and S. G. Love, "The Formation of Chondrules: Petrologic Tests of the Shock Wave Model," *Science,* vol. 280, no. 5360, pp. 62-67, 1998.

[14] R. A. Chevalier, "Interaction of Supernovae with Circumstellar Matter," in *Supernovae*, vol. XIII, A. G. Petschek, Ed., New York, Springer-Verlag, 1990.

[15] D. A. Leahy and R. S. Roger, "Radio Emission from the Supernova Remnant G160.9+2.6 (HB9)," *Astrophysical Journal,* vol. 101, no. 3, pp. 1033-1045, 1990.

[16] L. Deharceng, A. Zavagno, L. Salas, J. Porras, I. Caplan and Cruz-Gonzalez, "Sequential star formation at the periphery of the HII regions Sh 217 and Sh 219," *Astrophysics,* vol. 399, pp. 1135-1146, 2003.

[17] E. S. Agency, "Cosmos," European Space Agency, 2018. [Online]. Available: https://www.cosmos.esa.int/web/xmm-newton/technical-details. [Accessed 1 September 2018].

[18] S. Sara, S. Manami and D. Lorenzo, "XMM-Newton study of the Draco dwarf spheroidal galaxy," *Astronomy and Astrophysics,* vol. 586, no. A64, 2016.

[19] G. Giardino, F. Favata, G. Micela, S. Sciortino and E. Winston, "The onset of X-ray emission in young stellar objects: A Chandra observation of the Serpens star-forming region," *Astronomy & Astrophysics,* vol. 463, pp. 275-288, 2007.

[20] N. Chisari, *Propagation of Supernova Blast Waves through the ISM,* Department of Astrophysial Sciences, 2009.

[21] B. J. Kirby, Micro- and Nanoscale Fluid Mechanics: ransport in Microfluidic Devices, Cambridge University Press, 2009.

[22] CCDC, "https://www.ccdc.cam.ac.uk/structures/search?id=doi:10.5517/cc6ykwk&sid=DataCite," [Online]. Available: https://www.ccdc.cam.ac.uk/structures/search?id=doi:10.5517/cc6ykwk&sid=DataCite.

[23] F. C. Adams and F. H. Shu, "Infrared Spectra of Rotating Protostars," *Astrophysical Journal,* vol. 308, pp. 836-853, 1986.

[24] K. V. Getman, E. D. Feigelson, G. Garmire, P. Broos and J. Wang, "X-Ray Study of Triggered Star Formation and Protostars in IC 1396N," *Astrophysical Journal,* vol. 654, pp. 316-337, 2007.

[25] T. P. Robitaille, B. A. Whitney, R. Indebetouw, K. Wood and D. Pia, "Interpreting Spectral Energy Distributions from Young Stellar Objects. I. A Grid of 200,000 YSO Model SEDs," *Astrophysical Journal. Supplement Series,* vol. 167, pp. 256-285, 2006.

[26] S. Sharma, A. K. Pandey, D. K. Ojha, H. Bhatt, K. Ogura, N. Kobayashi, R. Yadav and J. C. Pandey, "The Stellar Contents and Star Formation in the NGC 7538 Region," *MNRAS,* vol. 000, pp. 1-25, 2016.

[27] I. P. Shkarofsky, T. W. Johnston and M. P. Bachynski, The Particle Kinetics of Plasmas, Addison-Wesley; 1st Edition edition, 1966.

[28] N. E. Chisari, *Propagation of Supernova Blast Waves through the,* Department of Astrophysical Sciences, 2009.

[29] R. Bedogni and P. R. Woodward, "Shock Wave Interactions with Interstellar Clouds," *Astronomy & Astrophysics,* vol. 231, pp. 481-498, 1990.

[30] D. A. Williams, "Gas and Dust in the Interstellar Medium," *Journal of Physics: Conference Series,* vol. 6, pp. 1-17, 2005.

[31] A. Telleschi, M. Guedel, K. R. Briggs, M. Audard and F. Palla, "X-ray Emission from T Tauri Stars and the Role of Accretion: Inferences from the XMM-Newton Extended Survey of the Taurus Molecular Cloud," *Astronomy & Astrophysics manuscript no. accretion,* 2018.

[32] T. Preibisch, Y.-C. Kim, F. Favata, E. D. Feigelson, E. Flaccomio, K. Getman, G. Micela, S. Sciortino, K. Stassun, B. Stelzer and H. Zinnecker, "The Origin of T Tauri X-ray Emission: New Insights from the Chandra Orion Ultradeep Project," *Astrophysics Journal Supplementary,* vol. 160, pp. 401-422, 2004.

[33] T. Montmerle and N. Grosso, "X-rays from Young Stellar Objects: Magnetic Structures and Irradiation Effects," in *Star Formation,* Nagoya, Japan, 1999.

[34] Povich, Smith, Majewski, Getman, T. Babler, Broos, Indebetouw, Meade, Robitaille, Stassun, Whitney, Yonekura and Fukui, "A PAN-CARINA YSO CATALOG: INTERMEDIATE-MASS YOUNG STELLAR OBJECTS IN THE CARINA," *Astrophysical Journal. Sypplement Series*, 2011.

[35] W. Forman, E. Kellogg, H. Gursky, H. Tananbaum and R. Giacconit, "Observations of the Extended X-Ray Sources in the Perseus and Coma Clusters from UHURU," *Astrophysical Journal*, vol. 178, pp. 309-316, 1972.

[36] S. Ueno, K. Koyama, H. Awaki, I. Hayashi and P. R. Blanco, "Detection of Hard X-Ray Emission from Mkn 463," *Astronomical Society of Japan*, vol. 48, no. 3, pp. 389-394, 1996.

[37] D. A. Leahy and W. W. Tian, "Radio spectrum and distance of the SNR HB9," *Astronomy and Astrophysics*, vol. 461, pp. 1013-1018, 2007.

[38] D. Cohen, M. Leutenegger, K. Grizzard, C. Reed, R. Kramer and S. Owocki, "Wind signatures in the X-ray emission-line profiles of the late-O supergiant Orionis," *Monthly Notices of the Royal Astronomical Society*, vol. 368, no. 4, pp. 1905-1916, 2006.

This publication makes use of data products from the Two Micron All Sky Survey, which is a joint project of the University of Massachusetts and the Infrared Processing and Analysis Center/California Institute of Technology, funded by the National Aeronautics and Space Administration and the National Science Foundation.

This work has made use of data from the European Space Agency (ESA) mission Gaia (https://www.cosmos.esa.int/gaia), processed by the Gaia Data Processing and Analysis Consortium (DPAC, https://www.cosmos.esa.int/web/gaia/dpac/consortium). Funding for the DPAC has been provided by national institutions, in particular the institutions participating in the Gaia Multilateral Agreement.

Appendix A

Table 4: Data file for all detected source across the four observations. Sources that show >35 counts but are not included in the analysis were either bad pixels or were located along the edges of the CCDs and were deemed contamination. The instrument identification numbers are as follows: PN=1, MOS1=2, MOS2=3. Sources that report 0 counts during an observation were not detected above the likelihood threshold. Their upper limits were computed and shown in Appendix C.

Source	Instrument ID	Coordinates	Counts				Optical Photometric Data					NIR Photometric Data			Classification
			Obs. 1	Obs. 2	Obs. 3	Obs. 4	g	r	i	z	y	J	H	K	
1	1		72	80	19	114									
1	2	4:56:05.601, +47:20:41.62	44	42	16	57	14.71	14.13	13.88	13.73	13.63	12.71	12.28	12.14	Main sequence
1	3		26	45	19	46									
2	1		54	86	0	151									
2	2	4:56:45.885, +47:11:21.90	29	44	0	34	21.43	21.65	21.10	20.20	19.71	-	-	-	YSO candidate
2	3		43	27	0	70									
3	1		67	143	20	61									
3	2	4:55:31.627, +47:12:11.76	26	66	23	40	11.0*	10.6*	10.5*	10.4*	10.4*	9.46	9.15	9.06	Main sequence
3	3		29	38	11	44									
4	1		28	0	0	0									
4	2	4:56:09.692, +47:22:26.55	0	0	0	0	21.50	19.80	18.98	18.37	17.89	16.39	15.28	14.72	Unclassified
4	3		19	0	0	0									
5	1		29	0	0	0									
5	2	4:56:45.055, +47:10:09.47	0	0	0	0	-	-	-	-	-	-	-	-	YSO candidate
5	3		18	0	0	0									
6	1		20	0	0	0									
6	2	4:56:10.691, +47:17:25.19	24	0	0	0	21.61	20.25	18.80	18.10	17.72	16.46	16.04	15.58	Main sequence
6	3		9	0	0	0									
7	1		62	70	0	0									
7	2	4:56:03.733, +47:22:47.58	0	0	0	0	19.92*	20.22	19.27	18.51	17.89	14.87*	14.80	14.29	YSO candidate
7	3		40	92	0	0									
8	1		19	30	0	39									

8	2	4:56:24.639, +47:13:50.48	18	19	0	13	-	-	21.00	20.55	-	-	-	-	Unclassified
8	3		10	18	0	34									
9	1		14	0	0	20									
9	2	4:56:45.404, +47:15:57.42	17	0	0	15	-	21.43	20.81	20.45	20.20	-	-	-	YSO candidate
9	3		9	0	0	26									
10	1		19	0	39	50									
10	2	4:56:47.619, +47:21:50.51	5	0	23	38	19.04	17.76	16.35	15.69	15.36	14.13	13.44	13.17	Unclassified
10	3		15	0	15	38									
11	1		0	37	0	53									
11	2	4:55:51.325, +47:13:06.45	0	27	0	42	14.82	13.81	13.36*	12.96*	12.80	11.53	10.93	10.73	Unclassified
11	3		0	27	0	23									
12	1		0	33	0	46									
12	2	4:57:20.125, +47:13:21.77	0	28	0	25	21.60	21.06	20.36	19.81	19.57	-	-	-	YSO candidate
12	3		0	20	0	33									
13	1		0	44	0	29									
13	2	4:56:29.481, +47:07:51.50	0	0	0	0	18.19	17.28	16.82	16.59	16.42	15.41	14.81	14.62	YSO candidate
13	3		0	25	0	41									
14	1		0	28	0	31									
14	2	4:55:59.866, +47:19:29.06	0	24	0	30	15.06	13.91	13.37	12.99	12.80	11.51	10.80	10.62	Unclassified
14	3		0	25	0	13									
15	1		0	4	0	0									
15	2	4:55:24.759, +47:06:55.63	0	26	0	16	-	-	-	-	-	-	-	-	Non-source
15	3		0	3	0	3									
16	1		0	13	0	0									
16	2	4:56:42.528, +47:20:24.83	0	15	0	0	8.74*	8.92*	9.10*	9.22*	9.28*	-	-	-	Main sequence
16	3		0	20	0	0									
17	1		0	0	9	32									
17	2	4:55:58.897, +47:19:56.09	0	0	8	16	-	-	-	-	-	-	-	-	Unclassified
17	3		0	0	21	30									
18	1		0	0	27	0									

18	2	4:55:51.687, +47:28:43.58	0	0	0	0	-	20.69	20.14	19.79	19.63	-	-	-	Non-source
18	3		0	0	13	0									
19	1		0	0	0	0									
19	2	4:55:44.290, +47:28:58.31	0	0	0	0	-	-	-	-	-	-	-	-	Non-source
19	3		0	0	0	66									
20	1		0	0	0	124									
20	2	4:55:30.308, +47:14:55.94	0	0	0	38	19.77	18.73	18.15	17.79	17.56	16.44	15.61	15.10*	YSO candidate
20	3		0	0	0	50									
21	1		0	0	0	44									
21	2	4:56:09.357, +47:21:51.96	0	0	0	0	15.12	13.93	13.67	12.66	12.48	11.27	10.65	10.45	Main sequence
21	3		0	0	0	32									
22	1		0	0	0	151									
22	2	4:55:43.293, +47:06:28.99	0	0	0	43	-	-	21.49	21.00	-				Non-source
22	3		0	0	0	6									

Figure 24 (a,b,c): Each of these figured were created using the MOS1, MOS2, and PN data during observation 1. (a, top left) HR_2/HR_1, (b, top right) HR_3/HR_2, (c, bottom left) HR_4/HR_3. The error bars for some sources extend past the area shown in the figures; however, a ratio greater than +1 or less than -1 does not make physical sense and so the graphs were cutoff at those limits.

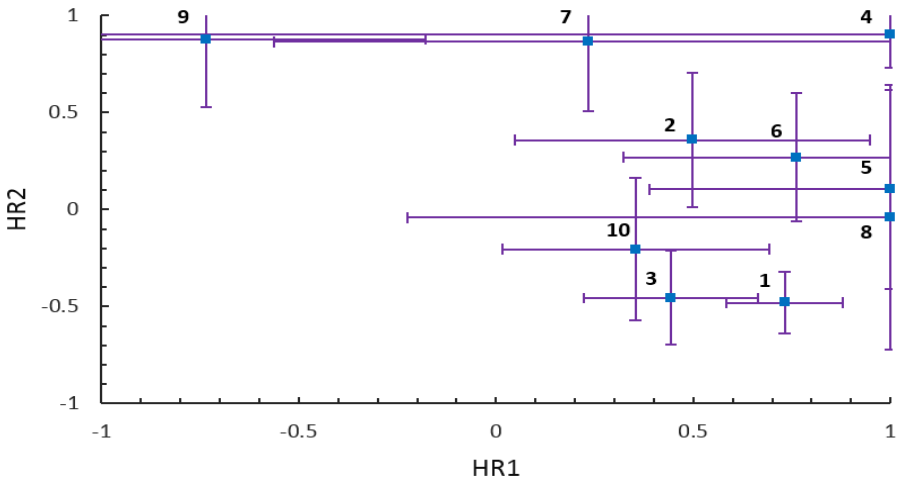

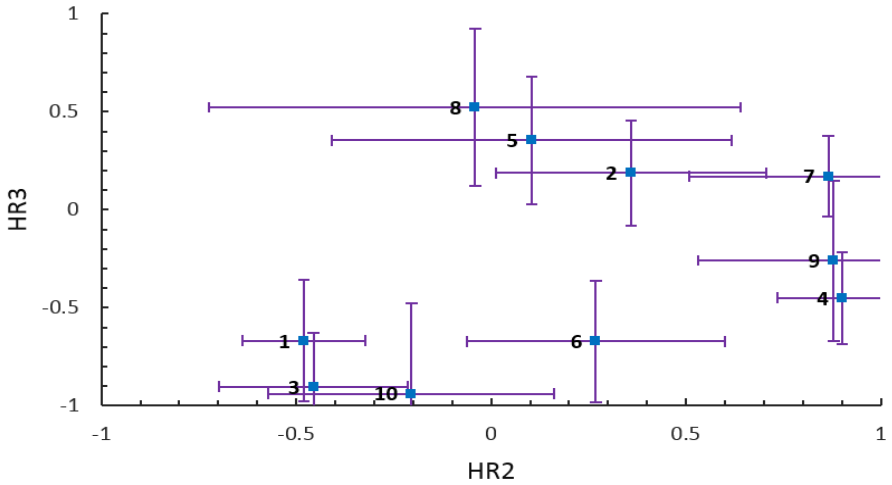

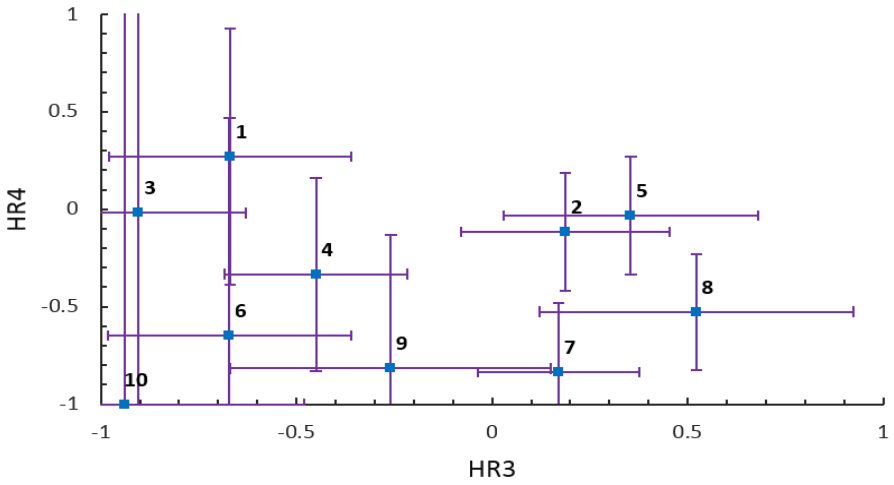

Figure 25 (a,b,c): Each of these figured were created using the MOS1, MOS2, and PN data during observation 2. (a, top left) HR_2/HR_1, (b, top right) HR_3/HR_2, (c, bottom left) HR_4/HR_3. The error bars for some sources extend past the area shown in the figures; however, a ratio greater than +1 or less than -1 does not make physical sense and so the graphs were cutoff at those limits.

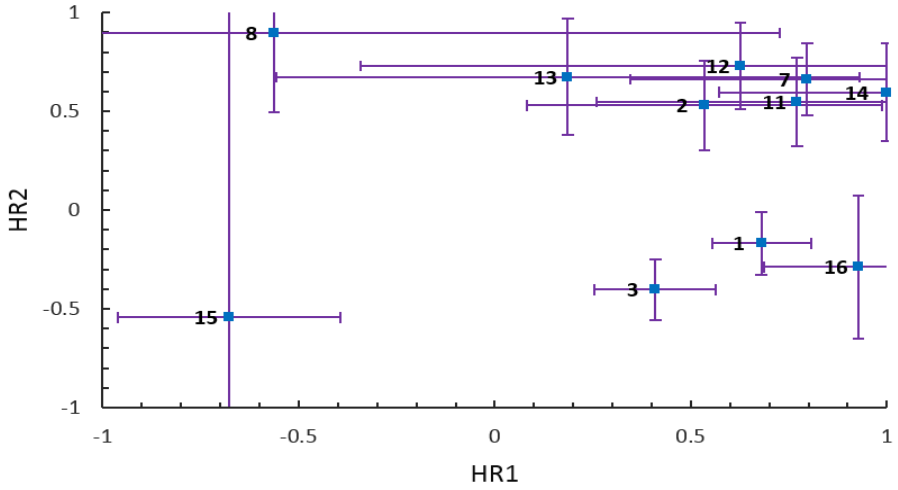

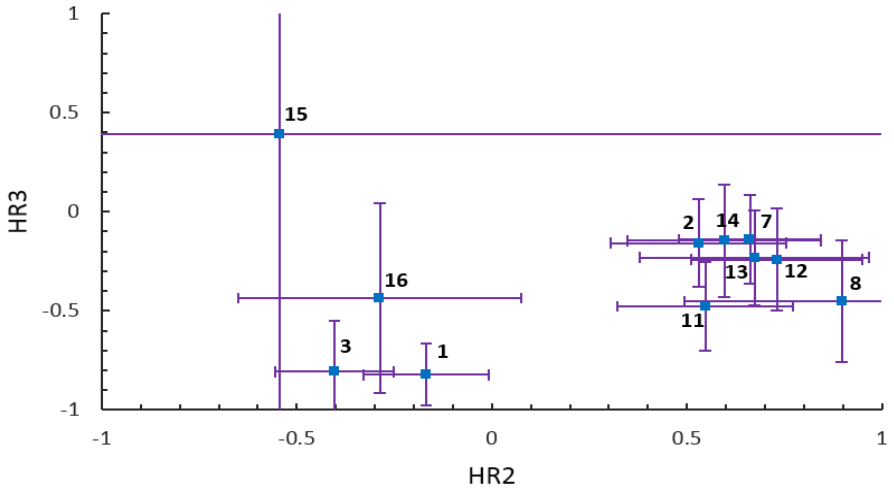

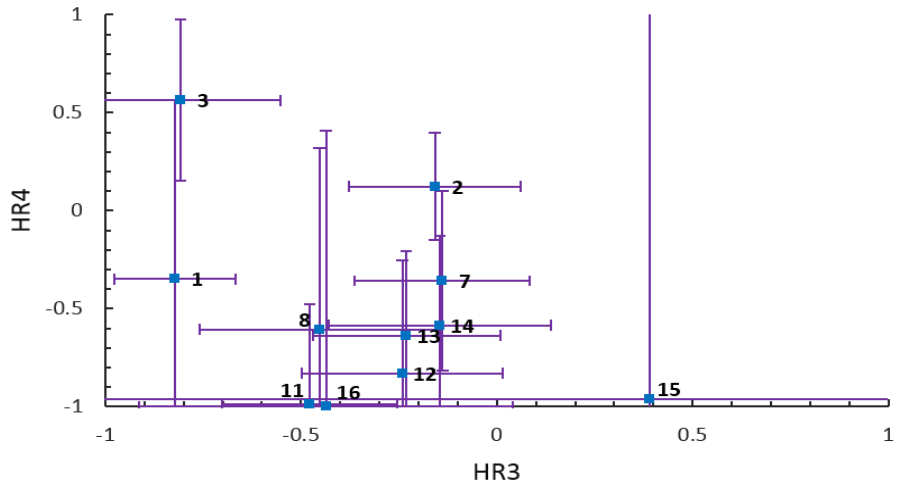

Figure 26 (a,b,c): Each of these figured were created using the MOS1, MOS2, and PN data during observation 3. (a, top left) HR_2/HR_1, (b, top right) HR_3/HR_2, (c, bottom left) HR_4/HR_3. The error bars for some sources extend past the area shown in the figures; however, a ratio greater than +1 or less than -1 does not make physical sense and so the graphs were cutoff at those limits.

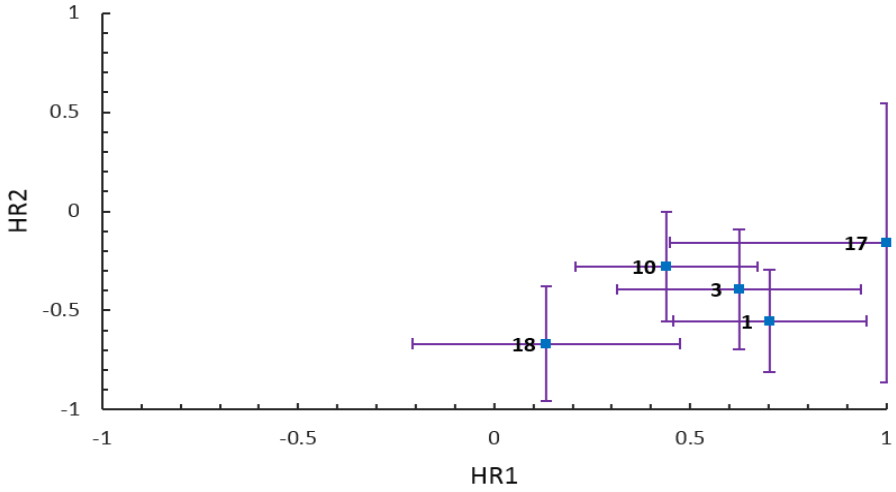

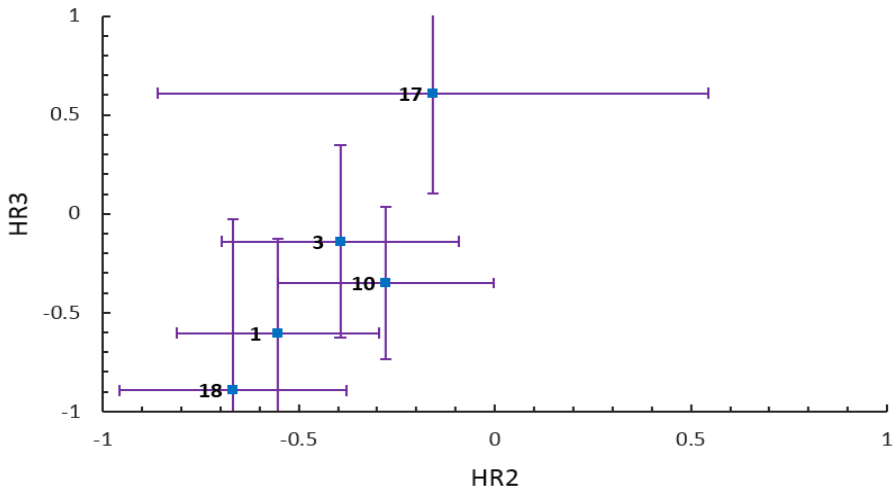

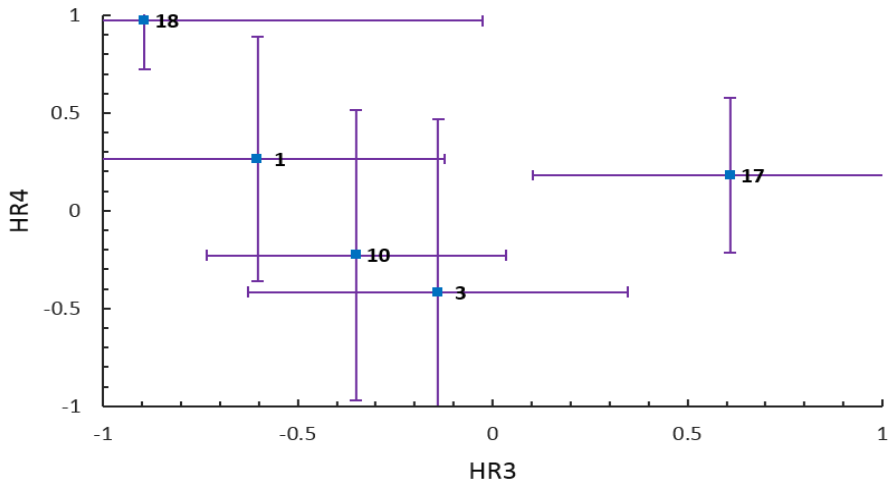

Figure 27 (a,b,c): Each of these figured were created using the MOS1, MOS2, and PN data during observation 4. (a, top left) HR_2/HR_1, (b, top right) HR_3/HR_2, (c, bottom left) HR_4/HR_3. The error bars for some sources extend past the area shown in the figures; however, a ratio greater than +1 or less than -1 does not make physical sense and so the graphs were cutoff at those limits.

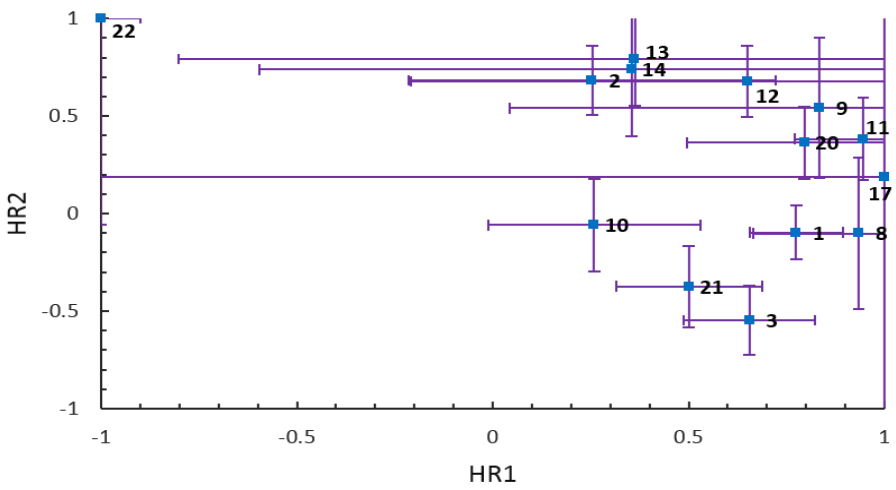

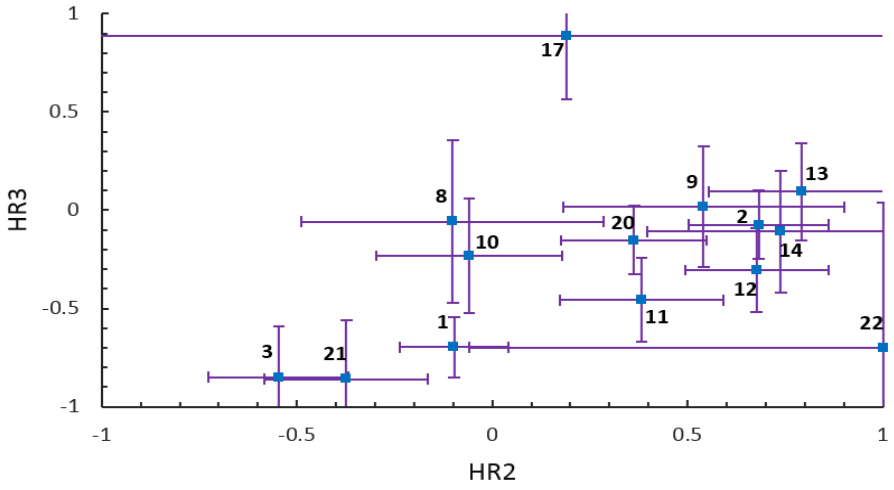

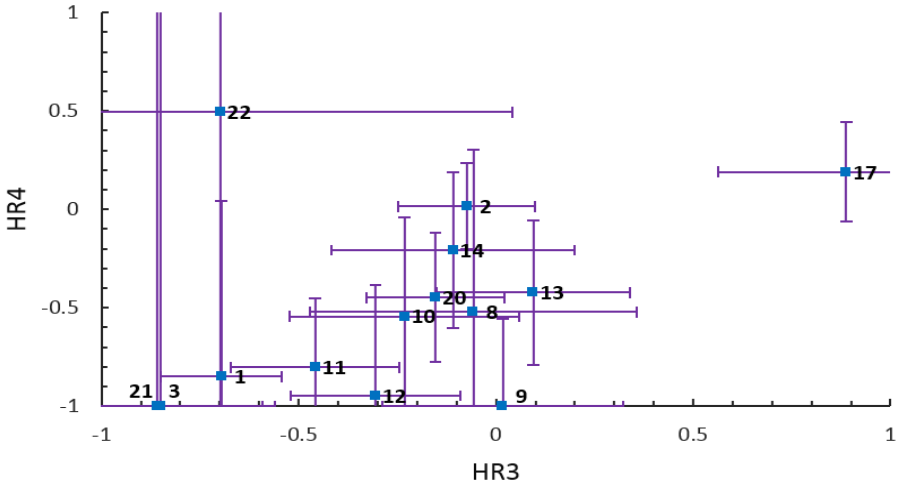

Appendix B

Table 5: Model fit parameters for the sources and observations with viable statistics. All spectra were fit with the *phabs*apec* model except for source 5 which had the *apec* model replaced with a simpler blackbody model (*bbody*). Errors that are marked with an asterisk could not have their 1σ range calculated and the reported value is the parameter uncertainty given by xspec.

Source	Observation	Hydrogen column density (10^{22}nH)	nH error range (1σ)	Plamsa temp. (keV)	Temp. error (1σ)	Metallicity abundance (solar fraction)	Normalization factor	$\frac{\chi^2}{ndof}$
1	1	0.0029	(0,0.19)	0.78	(0.56,0.84)	1	0.00000781	14.13/22
1	4	0.84	(0.72,0.94)	0.23	(0.18,0.28)	1	0.000553	32.43/31
2	2	1.37	(1.19,1.60)	0.85	(0.69,1.00)	0.3	0.000315	27.61/28
2	4	1.04	(0.64,1.32)	1.17	(1.00,1.61)	0.3	0.000167	41.7/42
3	1	0.59	(0.26,0.76)	0.2	(0.16,0.33)	1	0.000366	17.23/15
3	2	0.0000024	(0,0.11)	0.77	(0.71,0.83)	1	0.0000142	30.24/19
3	4	0.04184	(0,0.077)	0.65	(0.56,0.73)	1	0.00000880	19.64/22
5	1	0.00017	(0,1.09)	1.34	(0.95,1.79)	-	0.000000735	9.05/14
6	1	1.25	(0.96,1.51)	0.34	(0.25,0.48)	1	0.000212	20.19/19
8	4	insens.	-	3.82	(2.39,7.48)	1	0.0000229	33.88/34
8	4	insens.	-	2.49	(1.61,5.09)	0.3	0.0000282	32.88/34
9	4	2.52	(1.25,3.53)	1.08	(0.73,2.74)	0.3	0.000172	24.97/23
10	4	0.75	(0.49,0.98)	0.94	(±0.30)*	0.3	0.0000769	36.83/30
11	2	1.11	(+-0.52)*	1.7	(±0.51)*	1	0.0000524	31.82/29
12	2	0.94	(0.25,1.27)	1.30	(1.03,4.25)	1	0.0000915	25.75/22
12	2	0.54	(0.25,0.98)	1.56	(1.14,2.83)	0.3	0.000121	26.16/22
14	2	1.13	(0.83,1.40)	0.53	(0.41,0.74)	1	0.0000621	43.79/26
14	4	0.89	(0.46,2.91)	1.08	(0.58,1.33)	1	0.0000130	34.32/29
17	4	6.58	(4.46,10.09)	9.07	(5.09,24.1)	1	0.0000653	35.67/31
20	4	0.173	(0.08,0.30)	5.85	(3.39,13.1)	0.3	0.0000471	45.8/39
21	4	0.71	(0.51,0.90)	0.17	(0.13,0.22)	1	0.000475	16.09/15

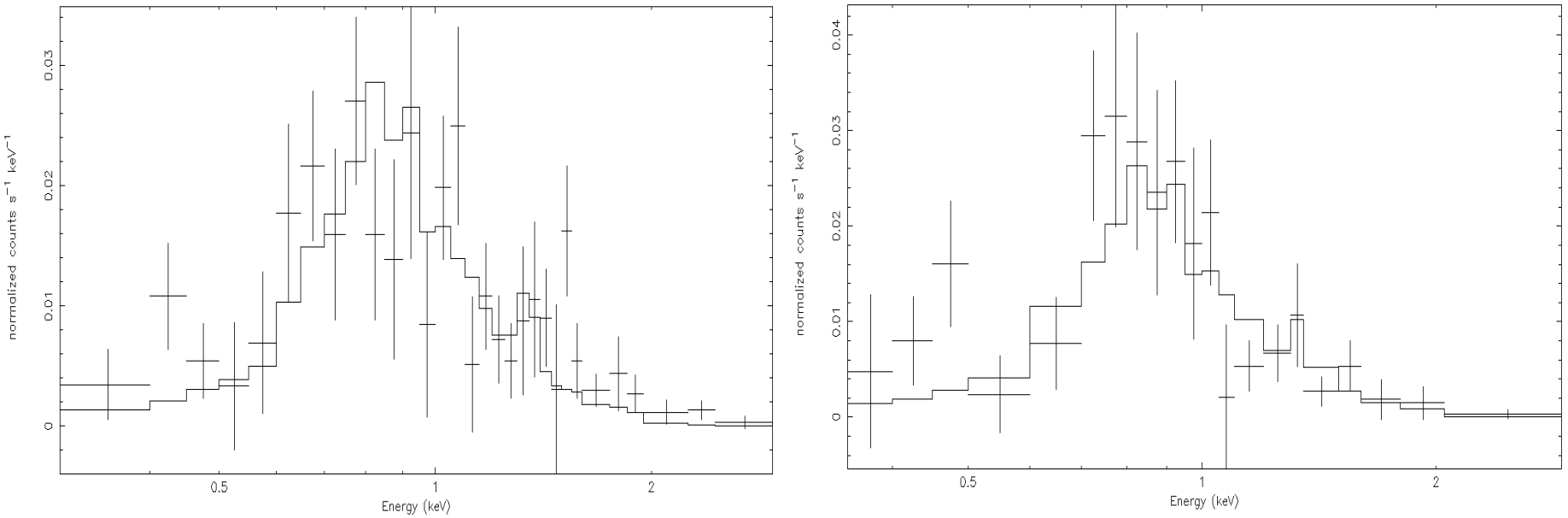

Figure 28: Spectrum and model fit corresponding to source 1 in observation 4 (left) and observation 1 (right).

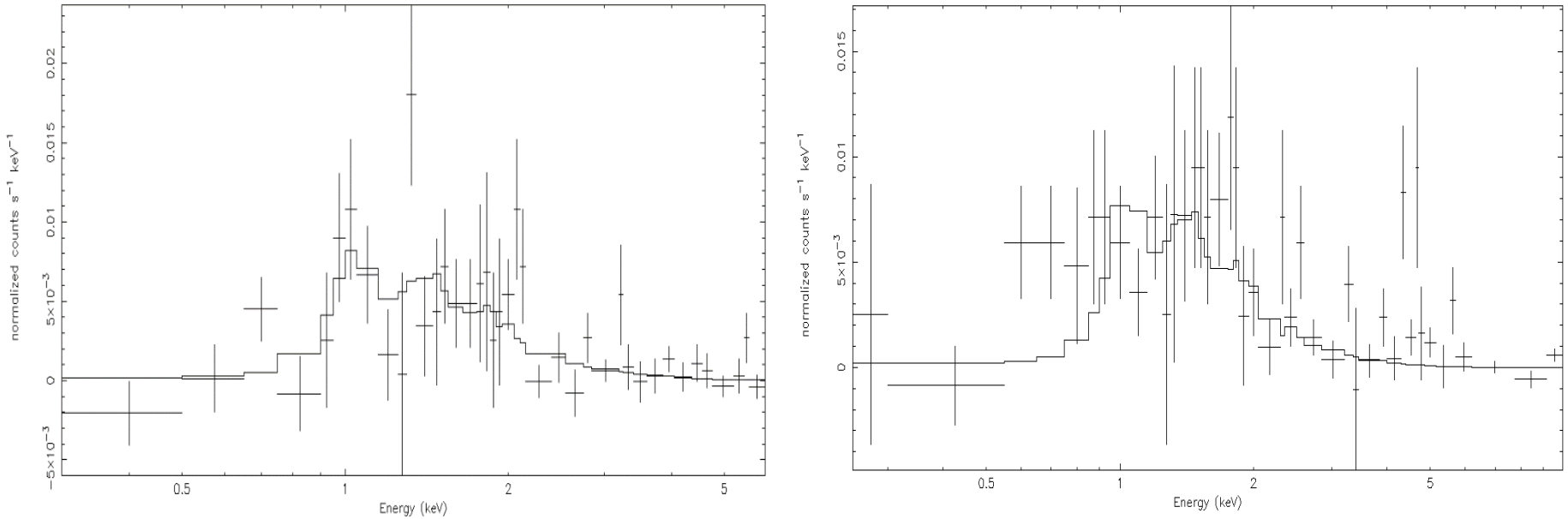

Figure 29: Spectrum and model fit corresponding to source 2 in observation 4 (left) and observation 2 (right).

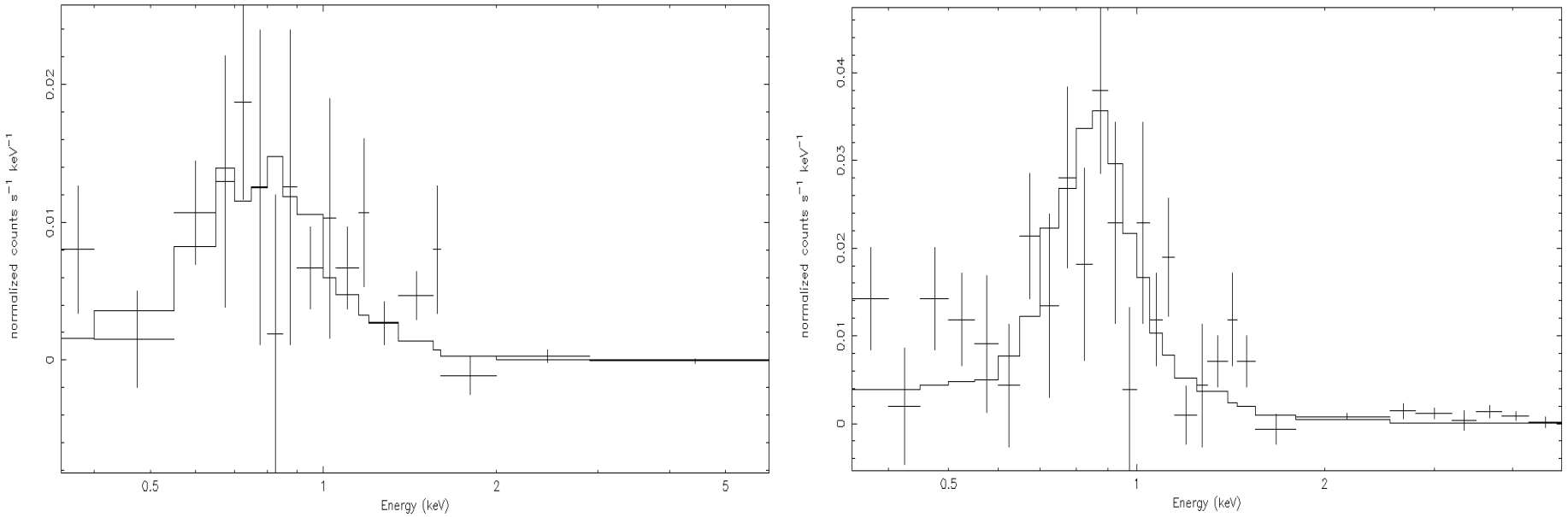

Figure 30: Spectrum and model fit corresponding to source 3 in observation 1 (left) and observation 2 (right).

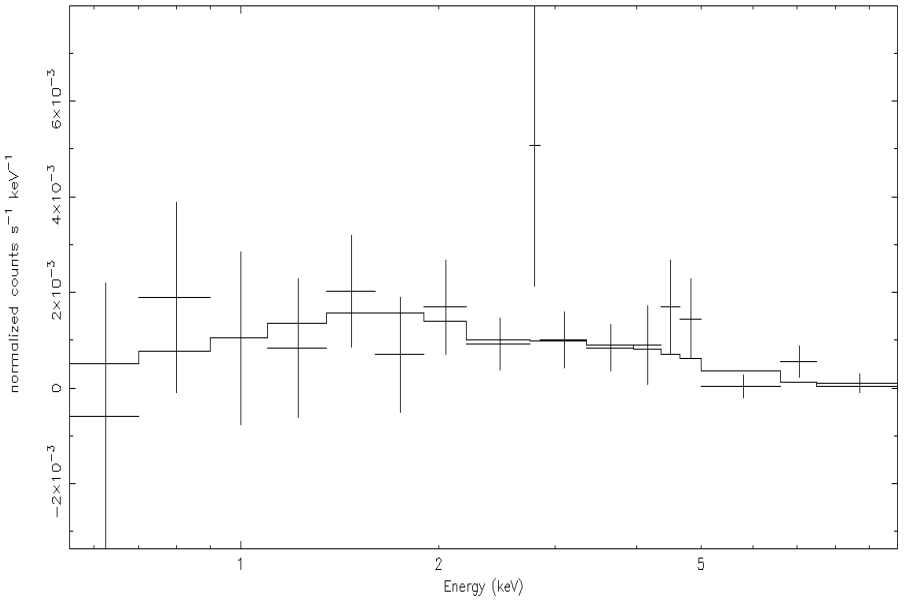

Figure 31: Spectrum and model fit corresponding to source 5 in observation 1. This spectrum was fit with a blackbody and absorption model as an approximation method due to low statistics.

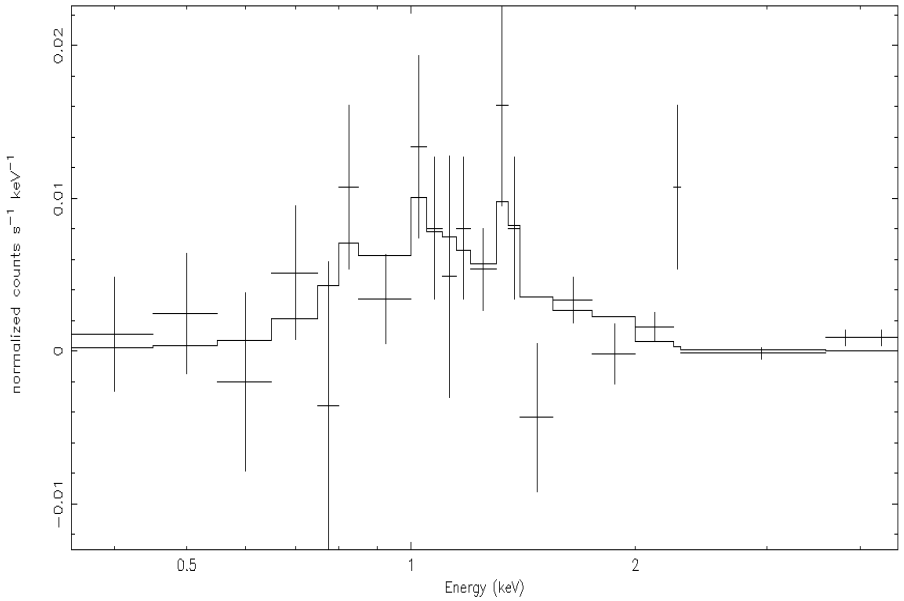

Figure 32: Spectrum and model fit corresponding to source 6 in observation 1.

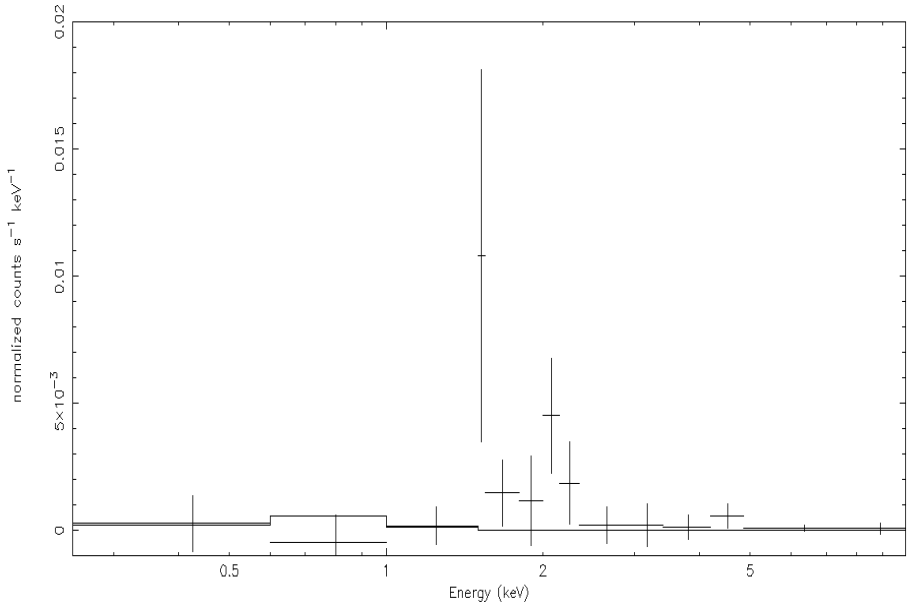

Figure 33: Spectrum and model fit corresponding to source 7 in observation 2. This source could not have its spectra fit due to low statistics. The fit line shown in the figure corresponds to the fit parameters of source 21 – a known MS foreground star. The model does not accurately capture harder X-rays in the 1.5-3.5 keV range suggesting that this source is not a MS star.

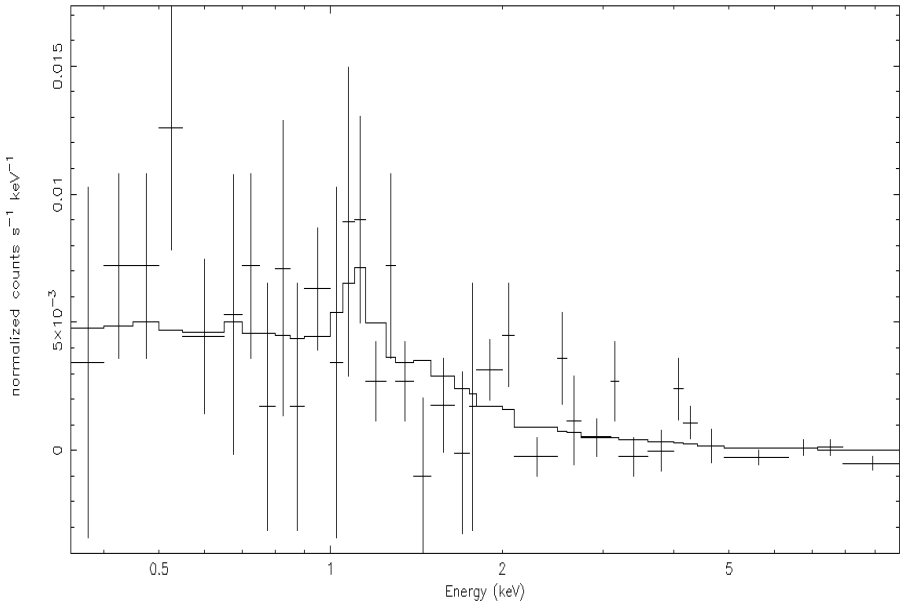

Figure 34: Spectrum and model fit corresponding to source 8 in observation 4. The fit was insensitive to the absorption parameter.

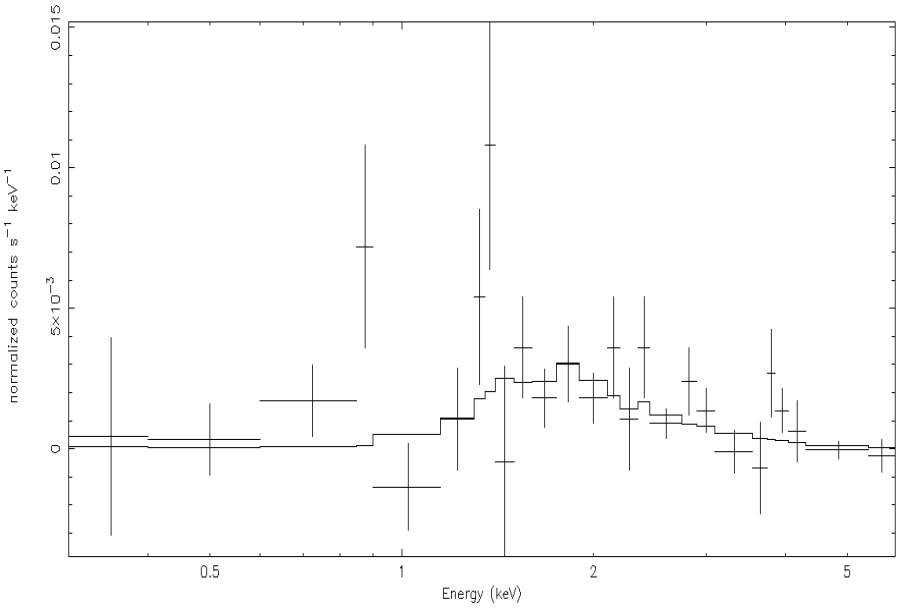

Figure 35: Spectrum and model fit corresponding to source 9 in observation 4.

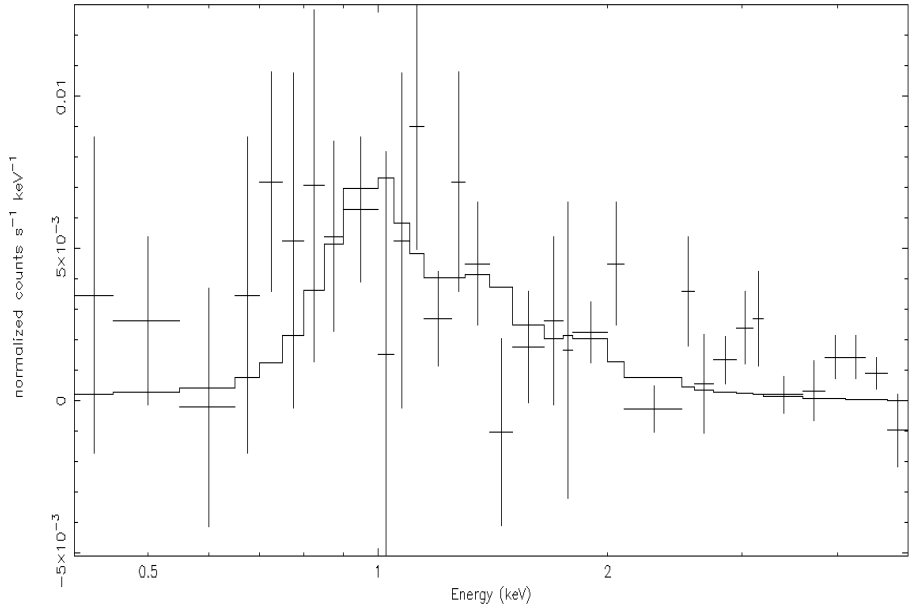

Figure 36: Spectrum and model fit corresponding to source 10 in observation 4.

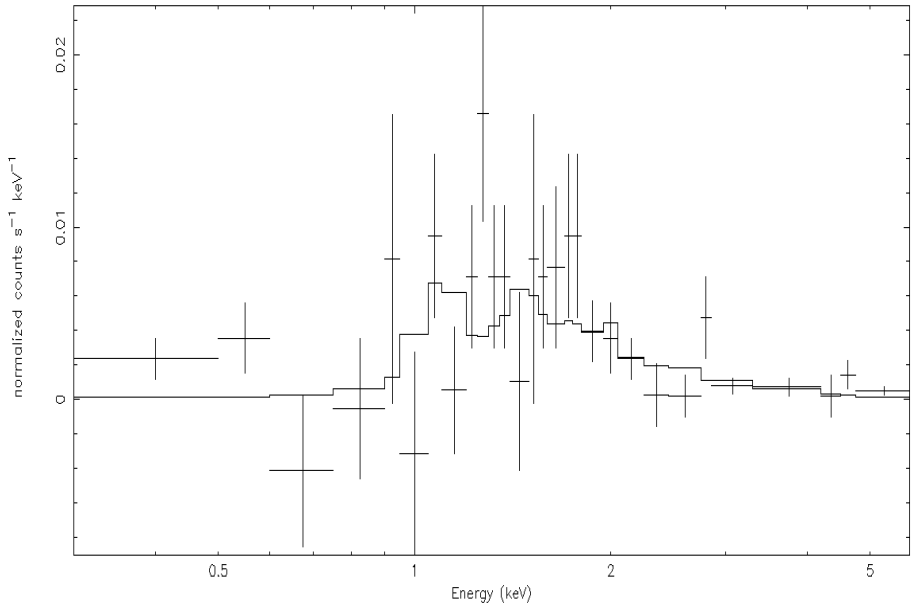

Figure 37: Spectrum and model fit corresponding to source 11 in observation 2.

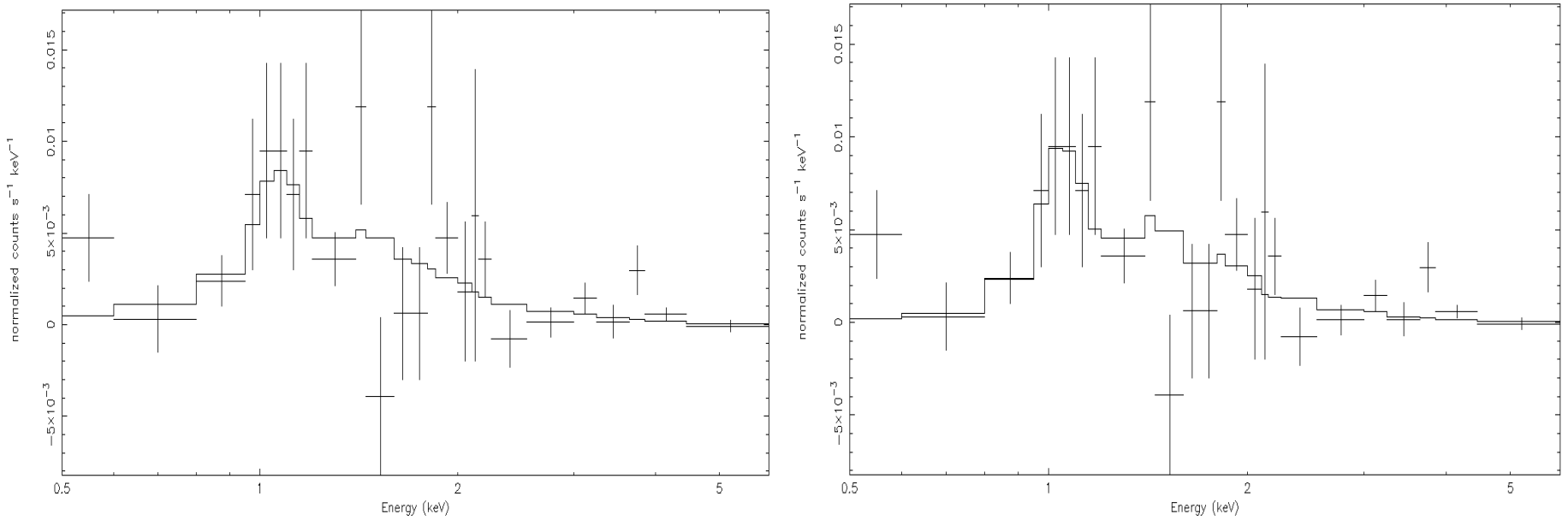

Figure 38: Spectrum and model fit corresponding to source 12 in observation 2. The left shows with fit with a metallicity abundance of 0.3 and the right image depicts the model fit with an abundance of 1.0.

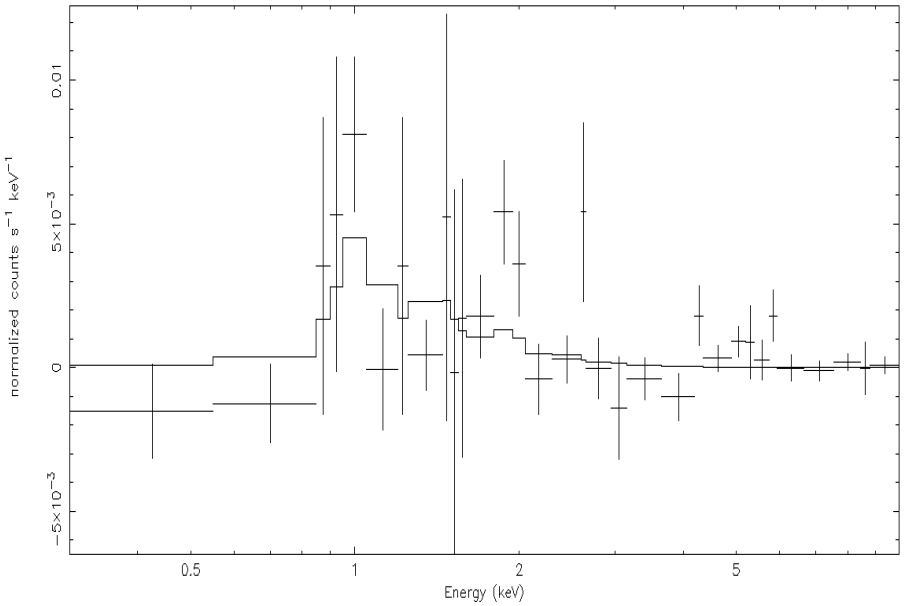

Figure 39: Spectrum and model fit corresponding to source 14 in observation 4.

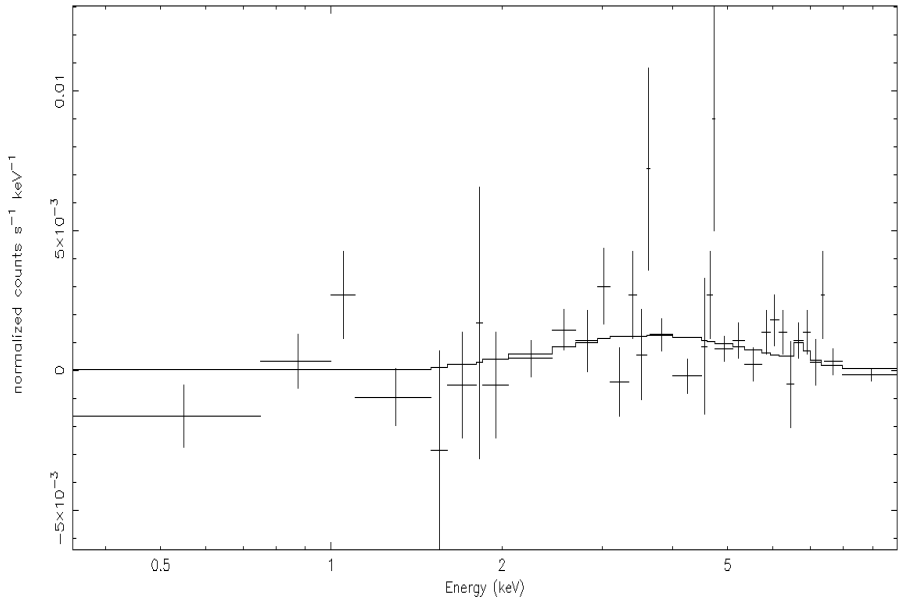

Figure 40: Spectrum and model fit corresponding to source 17 in observation 4.

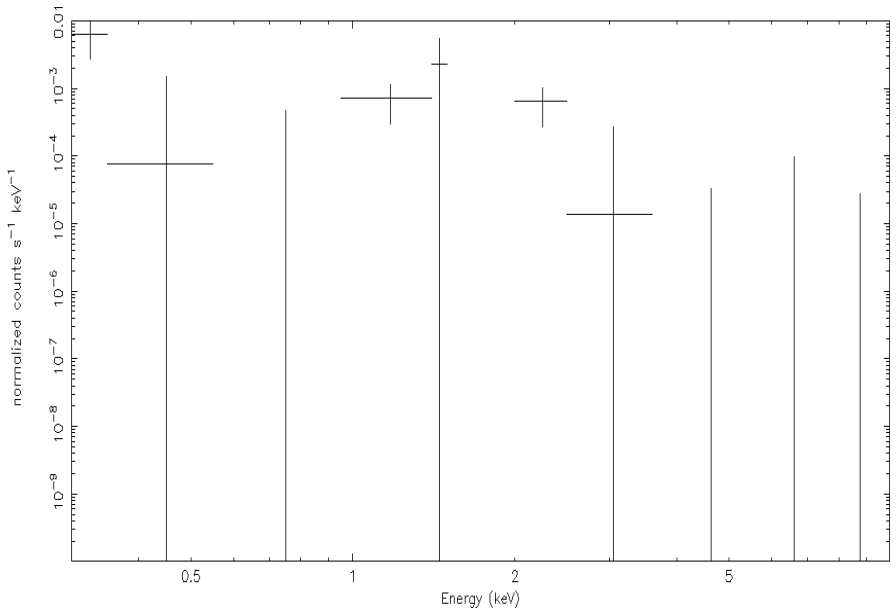

Figure 41: Spectrum corresponding to source 19 in observation 4 with logarithmic energy scale. The spectrum indicates that this is not an X-ray source and has its ounts dominated by low energy proton contamination. Furthermore, the background subtracted counts in the higher energy bins extremely low and are negative at times.

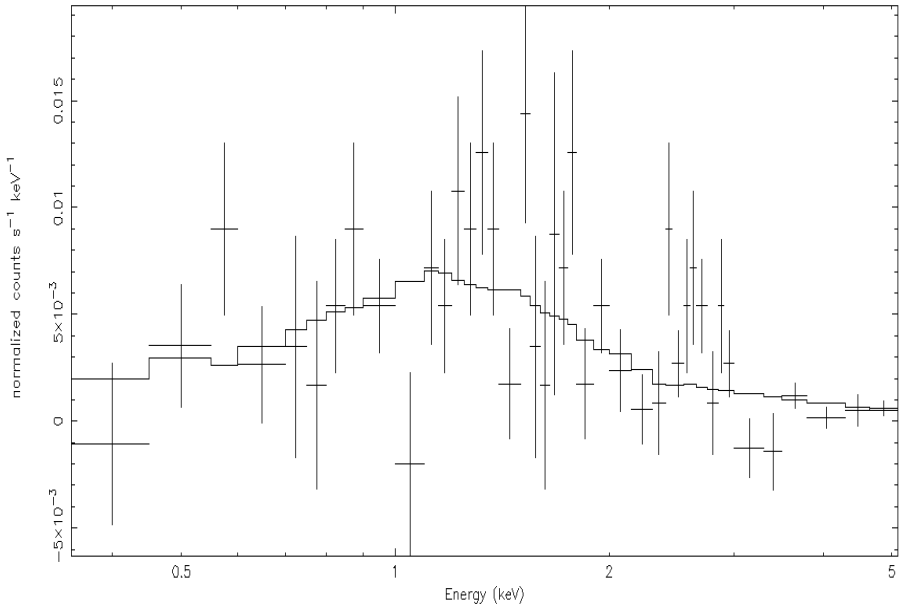

Figure 42: Spectrum and model fit corresponding to source 20 in observation 4.

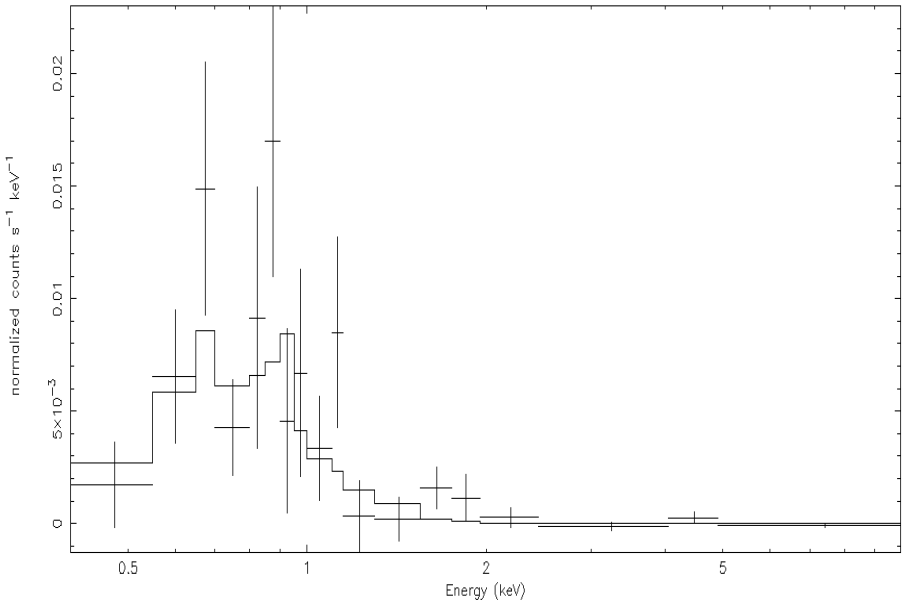

Figure 43: Spectrum and model fit corresponding to source 21 in observation 4.

Appendix C

Figure 44: Mean count numbers for each source across all 4 observations. To obtain the total counts simply multiple the shown value by three (averaged for MOS1 MOS2 and PN). Sources that were not detected in observations above threshold had their upper count limits calculated which are indicated by the downward arrows. Detected sources 18 and 19 could not have their upper limits calculated because of issues with the exposure mask around that area, however this is not an issue as these two were excluded from analysis and classified as non-sources.

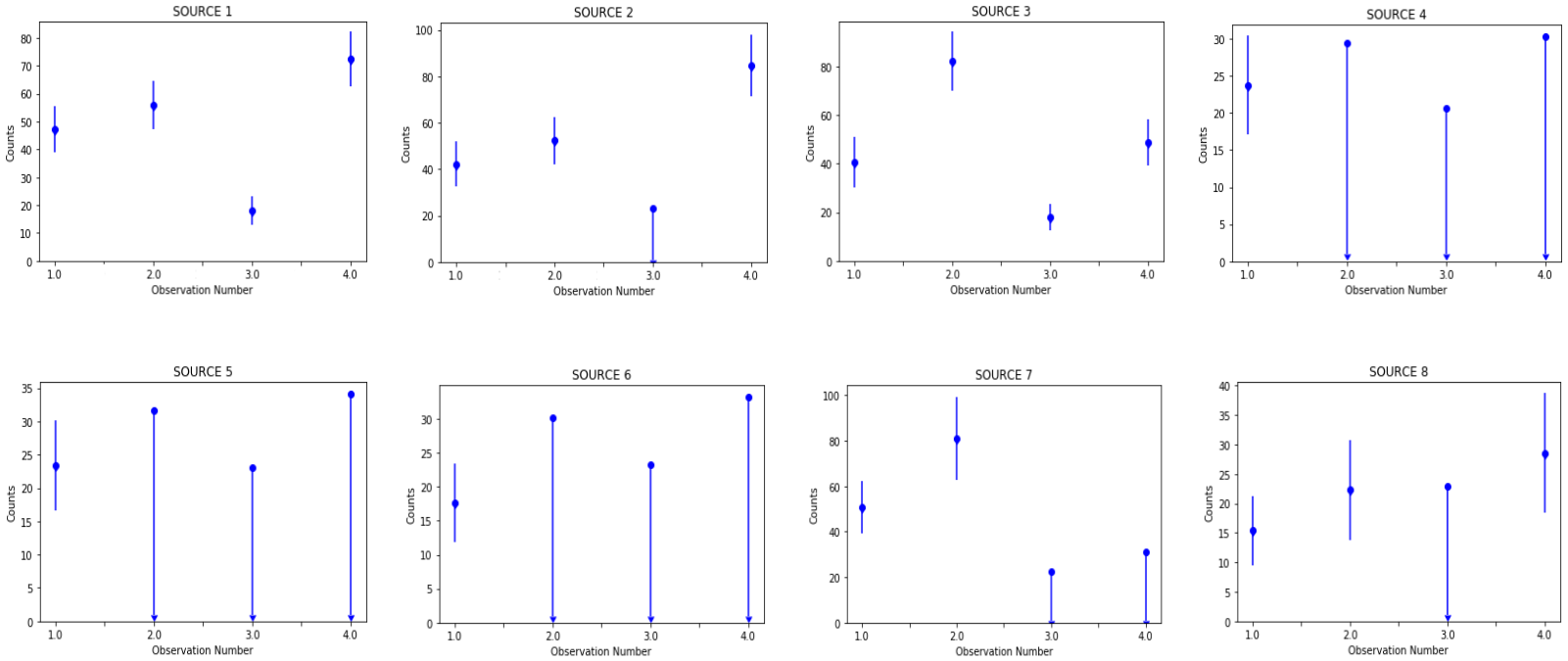

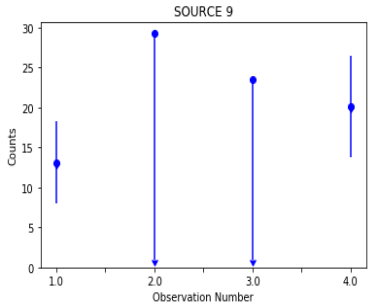
SOURCE 9
Counts
Observation Number

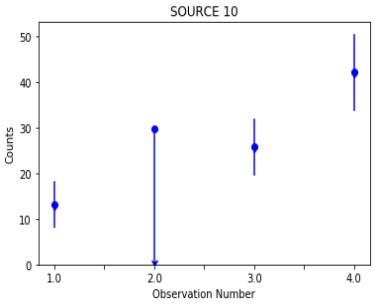
SOURCE 10
Counts
Observation Number

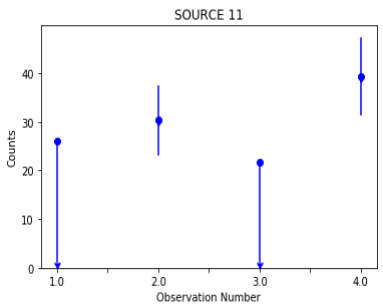
SOURCE 11
Counts
Observation Number

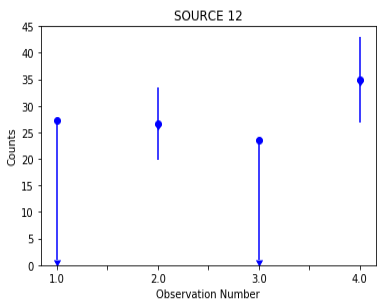
SOURCE 12
Counts
Observation Number

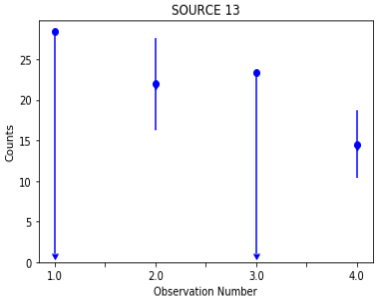
SOURCE 13
Counts
Observation Number

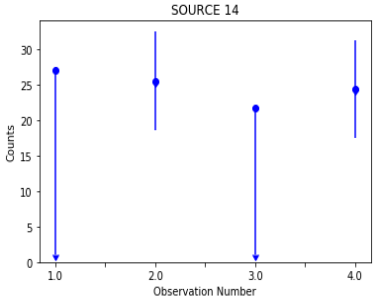
SOURCE 14
Counts
Observation Number

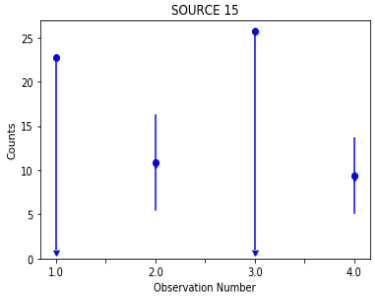
SOURCE 15
Counts
Observation Number

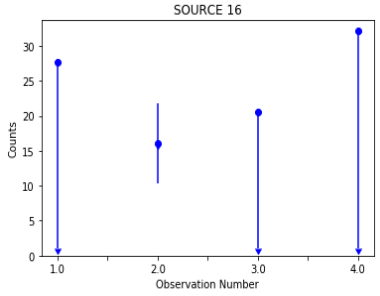
SOURCE 16
Counts
Observation Number

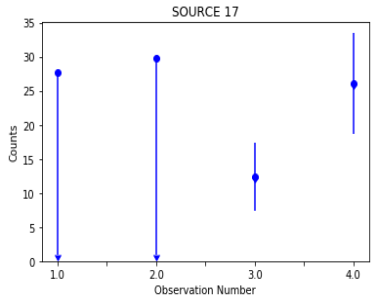
SOURCE 17
Counts
Observation Number

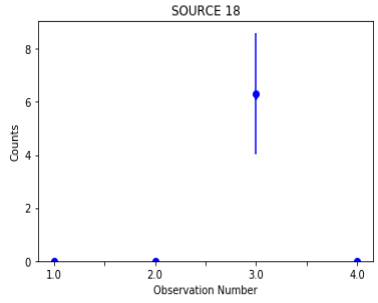
SOURCE 18
Counts
Observation Number

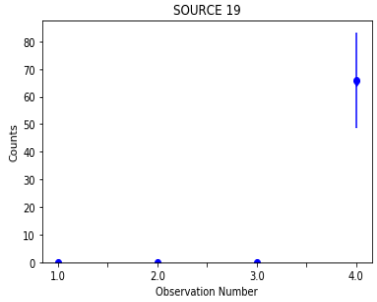
SOURCE 19
Counts
Observation Number

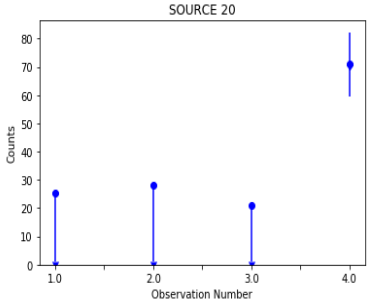
SOURCE 20
Counts
Observation Number

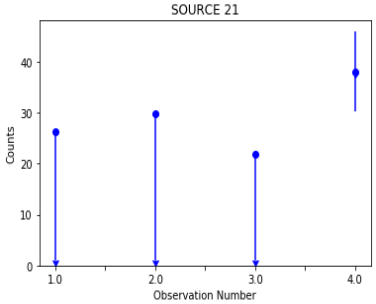
SOURCE 21
Counts
Observation Number
0
10
20
30
40
1.0
2.0
3.0
4.0

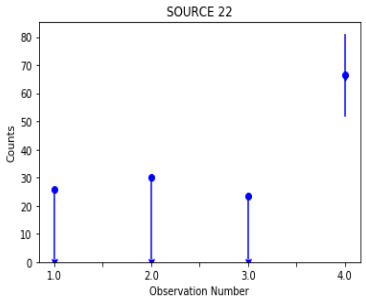
SOURCE 22
Counts
Observation Number
0
10
20
30
40
50
60
70
80
1.0
2.0
3.0
4.0